Effect of Ti and Nb addition on hot deformation and dynamic recrystallization modeling of boron-bearing low-carbon steel: A comparative study using hot compression flow curves

S.M. Mirghasemi*, E. Mohammad Sharifi[1]*, GH. Borhani*

*Malek Astar University of Technology, Department of Material Science and Advanced Material

Abstract

The hot deformation behavior modeling and microstructural evolution of low-carbon boron steels with Ti (FBT) and Nb (FBN) additions were investigated and compared with a baseline boron-treated steel (FB) in our previous work. Hot compression tests were conducted at temperatures of 850–1150 °C and strain rates of 0.01–10 s^{-1}. Flow curve analysis revealed that both Ti and Nb increased flow stress and delayed the onset of dynamic recrystallization (DRX), with the effect more pronounced in FBN. Constitutive analysis based on the Arrhenius model showed that the activation energy of deformation increased from 293.37 kJ/mol in FB to 314.15 kJ/mol in FBT and 353.04 kJ/mol in FBN, highlighting the strong pinning effect of precipitates. Critical stresses and strains (σ_c, σ_p, ε_c, ε_p) followed the order FB < FBT < FBN, indicating higher resistance to recrystallization in the microalloyed steels. DRX kinetics, modeled using the Avrami equation, yielded exponents of 2.09, 1.65, and 1.88 for FB, FBT, and FBN, respectively, confirming that Ti suppressed nucleation more strongly than Nb. Microstructural analysis demonstrated that Ti inhibited BN formation and promoted TiN/Ti(C,N), whereas Nb retained BN and generated Nb(C,N), mainly at MnS interfaces. Grain size distribution analysis revealed that both FBT and FBN exhibited significantly finer and more homogeneous grains compared to FB, with average grain sizes at 1150 °C (0.1 s^{-1}) of 17.3 μm in FBT and 17.0 μm in FBN, nearly half that of FB (33.6 μm). Overall, Ti and Nb additions distinctly altered the high-temperature deformation and recrystallization mechanisms of boron steels, enhancing grain refinement while suppressing DRX, thereby extending the findings of our previous study on FB.

Keywords: micro alloyed steel, boron bearing steel, Arrhenius relation, drx Avrami modeling

1. Introduction

The role of boron (B) in steels has been extensively investigated due to its pronounced effect on hardenability and microstructural evolution. In conventional boron-treated steels, the presence of boron at grain boundaries is well established to retard grain boundary migration and recrystallization, thereby enhancing strength and toughness [1] [2]. However, the addition of microalloying elements such as titanium (Ti) and niobium (Nb) substantially alters this behavior by modifying both the type and distribution of precipitates. Titanium exhibits a strong

[1] Corresponding author: e-m-sharifi@mut-es.ac.ir

[DOI: 10.22068/ijmse.4448]

affinity for nitrogen and boron, forming stable precipitates like TiN and Ti(C,N), which suppress the formation of BN and alter the availability of solute boron . Similarly, niobium contributes through the formation of Nb(C,N), which can significantly influence recrystallization kinetics and grain refinement. Therefore, investigating the combined effects of Ti and Nb with boron in these alloys provides critical insight into the interplay between precipitation, solute drag, and microstructural control [3] [4] [5].

At elevated temperatures, the thermomechanical response of these steels is strongly governed by the interaction between dislocation dynamics, precipitation, and restoration mechanisms. The addition of Ti and Nb is known to enhance the precipitation hardening effect, thereby delaying dynamic recrystallization (DRX) and favoring dynamic recovery (DRV) as the dominant softening mechanism [3] [4] [5] [6]. These precipitates not only pin dislocations and grain boundaries but also reduce the driving force for nucleation and growth of recrystallized grains, which can manifest as higher flow stresses, delayed critical strain, and smaller recrystallized fractions compared to Ti- and Nb-free steels. Such interactions are of particular importance in hot working processes, where flow behavior and DRX kinetics directly control grain size evolution and final mechanical properties [7] [8].

Given the complexity of these interactions, modeling approaches play an indispensable role in quantitatively assessing the effects of alloying additions. Constitutive modeling of high-temperature flow behavior, coupled with kinetic analysis of DRX using frameworks such as the Avrami equation, allows for the extraction of material constants that reveal the fundamental mechanisms controlling deformation. Through modeling, the influence of Ti and Nb on critical strain, peak strain, and recrystallization kinetics can be evaluated systematically, bridging experimental flow curves with microstructural outcomes. Moreover, predictive models offer valuable input for industrial process design, enabling optimized hot deformation schedules for steels containing boron and microalloying elements [9] [10].

Previous studies have investigated the role of Ti and Nb in microalloyed steels [3] [5] [11], as well as the impact of boron on transformation behavior. However, limited work has been done on boron-treated steels where Ti and Nb are added separately and in combination, particularly in the context of high-temperature deformation and DRX kinetics. In most cases, Ti and Nb have been studied in isolation or in steels without boron additions, leaving an important gap regarding their combined influence on the flow behavior, precipitation characteristics, and microstructural evolution of boron-treated steels. This motivates the present work, which aims to systematically compare three alloys: FB (boron-treated base steel), FBT (boron + Ti), and FBN (boron + Nb), in order to reveal how Ti and Nb distinctly modify the high-temperature deformation and recrystallization mechanisms.

Therefore, the objective of this study is to provide a comparative evaluation of the hot deformation behavior, DRX kinetics, and microstructural evolution of FB, FBT, and FBN alloys. The current work builds directly upon our earlier study [12], where the baseline behavior of FB was characterized in detail. By extending the investigation to FBT and FBN, we establish how Ti and Nb additions influence flow stress levels, critical parameters, and

[DOI: 10.22068/ijmse.4448]

microstructural outcomes at elevated temperatures. The combination of experimental hot compression tests, constitutive and kinetic modeling, thermodynamic simulations, and microstructural analyses offers a comprehensive framework to understand these effects. Ultimately, this work highlights the significance of Ti and Nb in tailoring the deformation response of boron-treated steels, providing insights valuable for both fundamental metallurgy and practical hot-working applications.

2. EXPERIMENTAL PROCEDURES

Alloy making

In our previous work [12], the base low-carbon boron-bearing steel FB was introduced and its chemical composition characterized. The same alloy was selected as the starting material for the present study. In order to investigate the effect of titanium and niobium additions, controlled amounts of these microalloying elements were incorporated into the FB steel.

In the previous work, the initial composition of FB was obtained by spark emission spectroscopy (SES) and inductively coupled plasma (ICP) analysis, repeated for accuracy. The steel contained 0.053 wt.% carbon and approximately 21 ppm boron, with about 23 ppm nitrogen—an unavoidable constituent in steelmaking that significantly influences precipitation and recrystallization behavior. As noted previously, the strong tendency of boron to form BN precipitates may diminish its beneficial role in improving mechanical properties. Thus, the addition of Ti and Nb was considered as a strategy to form more stable nitrides and carbonitrides (TiN, Nb(C,N)) and thereby prevent boron from combining with nitrogen, preserving its effectiveness in solid solution.

The main objective of alloying FB with Ti and Nb was to create thermodynamic conditions favoring stable nitride/carbonitride formation, more stable than BN, and thus maintain the active boron fraction. To identify suitable Ti and Nb levels, thermodynamic simulations were performed using JMatPro software. The stability range of austenite was chosen as the evaluation window, since boron segregation primarily occurs in this temperature interval. The equilibrium calculations indicated that in the austenite field the possible precipitates were MnS, BN, TiN, and TiB_2, with boron carbides of the $M_{23}(B,C)_6$ type forming near the upper end of the range. In the ferrite field, cementite appeared together with AlN and Nb(C,N) precipitates. It was estimated that only about 4 ppm of boron remained in solid solution under equilibrium conditions.

To suppress BN precipitation, Ti and Nb additions were hypothetically introduced in the thermodynamic calculations. The results (Figures 1 and 2) showed that increasing Ti content promoted TiN formation while reducing BN; at ~0.015 wt.% Ti, BN was completely eliminated. In contrast, Nb promoted the formation of Nb(C,N) but had little effect on BN stability. According to previous reports, Nb(C,N) particles can strongly influence dislocation

[DOI: 10.22068/ijmse.4448]

mobility, grain boundary motion, and consequently the recrystallization behavior, while also encouraging boron carbide precipitation along prior austenite grain boundaries. For comparison, Nb was considered in the same compositional range as Ti.

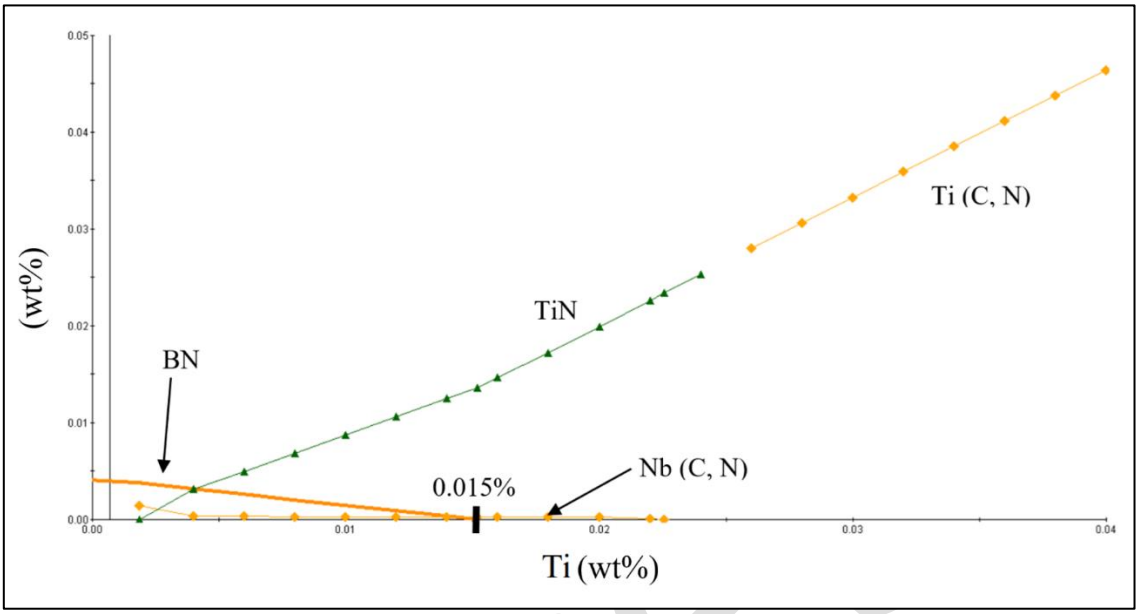

Figure 1. Effect of Ti addition on the BN content.

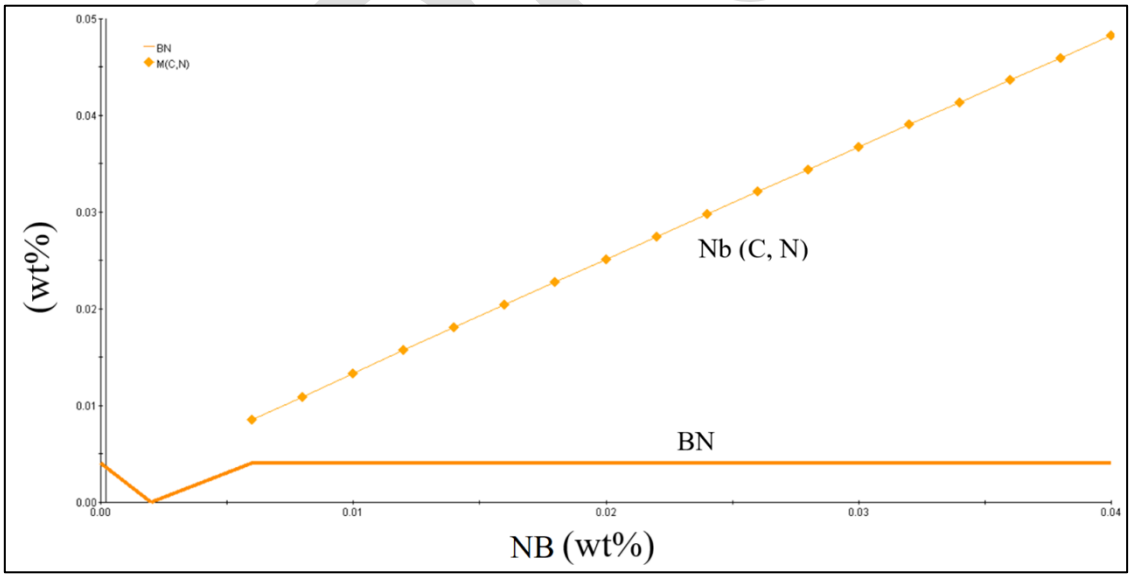

Figure 2. Effect of Nb addition on the BN content.

To validate the JMatPro results, literature data on Ti- and Nb-microalloyed low- and medium-carbon steels with similar chemical composition were reviewed. As summarized in Table 1, the recommended additions generally fall within 0.012–0.042 wt.% for Ti and 0.007–0.043 wt.% for Nb. Based on both simulation and literature data, target alloying ranges of 0.02–0.04 wt.% for each element were selected in this study.

[DOI: 10.22068/ijmse.4448]

Table 1. Chemical composition of steels reported in similar studies.

	reference	year	wt.%				ppm		wt.%	
			C	Mn	Si	Al	N	B	Ti	Nb
1	Ronchiato et. al. [13]	1985	0.31	1.4	0.28	0.048	-	29	0.037	-
2	Perez et. al. [14]	1993	0.24	1.33	0.158	0.043	39	15	0.013	-
3	Juarez et. al. [15]	1994	0.24	1.33	0.158	0.043	39	15	0.013	-
4	Seto et. al. [16]	1999	0.002	0.16	0.01	-	25	22	0.04	0.007
5	Kim et. al. [17]	2001	0.081	0.947	0.14	0.03	55	20	-	0.02
6	Jun et. al. [18]	2006	0.053	1.9	0.25	-	40	15	0.067	
7	Saha et. al. [19]	2007	0.004	0.12	0.01	0.04	33	9	0.042	0.042
8	Hwang et. al. [20]	2011	0.1	1.5	0.3	0.3	-	22	0.016	-
9	Kim et. al. [21]	2012	0.003	1.1	-	0.035	30	30	0.018	0.038
10	Terzic et. al. [22]	2013	0.07	1.3	0.25	0.03	35	30	0.012	0.012
11	Guler et. al. [2]	2014	0.19	1.13	0.65	-	-	30	0.033	-
12	Zhang et. al. [23]	2014	0.1	1.7	0.345	-	-	20	0.034	-
13	Li et. al. [24]	2015	0.19	1.2	0.35	0.06	-	12	-	0.03
14	Murari et. al. [6]	2015	0.1	1.8	0.5	0.025	42	27	0.028	
15	Shi et. al. [11]	2020	0.077	1.21	0.2	0.011	90	30	0.015	-

The alloys were then produced by vacuum induction melting (VIM) and alloying, followed by composition verification using SES analysis and ICP (Table 2). The boron content was kept within 15–20 ppm, which is considered optimal for mechanical performance. Notably, aluminum was removed from the composition of the new alloys, and small changes were observed in some other minor elements. These variations, together with Ti and Nb additions, are expected to influence the nature of precipitates and thereby affect the microstructural evolution and mechanical behavior. Notable precipitates based on Thermodynamic evaluations of the modified alloys are presented in the Results section.

[DOI: 10.22068/ijmse.4448]

Table 2. Chemical composition of the investigated steels (FB from [12]).

wt. %	FB	FBT	FBN
Fe	base	base	base
C	0.053	0.05	0.045
Si	0.007	0.01	0.01
Mn	0.477	0.44	0.42
P	0.007	0.007	0.008
S	0.003	0.002	0.004
Cr	0.009	0.006	0.01
Mo	0.001	0.007	0.007
Ni	0.023	0.02	0.02
V	0.003	0.002	0.003
Cu	0.007	0.003	0.005
Al	0.039	-	-
Nb	0.0002	0.002	0.030
Ti	0.0007	0.025	-
N (ppm)	23	23	25
B (ppm)	21	17	15

Hot Compression Testing and Data Processing

To investigate the hot deformation behavior and dynamic recrystallization of the alloys, hot compression tests were performed and the corresponding true stress–strain flow curves were obtained.

Cylindrical specimens with 5 mm diameter and 10 mm height were machined from the cast ingots by wire cutting, following the procedure described in our previous work in accordance with ASTM-E9. Tests were conducted at four temperatures (850, 950, 1050, and 1150 °C) and four strain rates (0.01, 0.1, 1, and 10 s^{-1}) using a DIL 805A/D dilatometer (Bähr, Germany). Each specimen was first heated to 1200 °C and held for 5 min to homogenize, then cooled at 5 °C/s to the testing temperature, deformed to 50% height reduction at the selected strain rate, and finally quenched. The thermomechanical condition is illustrated schematically in our previous work [12].

After deformation, the specimens were sectioned along the axis, mounted, ground, polished, and etched for microstructural analysis using optical microscopy (OM) and scanning electron microscopy (SEM) and Energy Dispersive Spectroscopy (EDS).

As in our earlier work, two corrections were applied to the raw stress–strain data to improve accuracy: Friction correction, to eliminate the effect of barreling, the stress values were

[DOI: 10.22068/ijmse.4448]

corrected using the well-established relationships [25] [26] [27]; and Adiabatic heating correction, to compensate for temperature rise during deformation, the true stress values were adjusted using the classical energy balance approach. In this method, the efficiency factor η was used to account for heat transfer to the dies. The resulting temperature rise was translated into a stress correction.

For mathematical Treatment and Curve Fitting, Critical strain for dynamic recrystallization was determined using the strain-hardening rate ($\theta = d\sigma/d\varepsilon$) method. The criterion is based on locating the zero crossing of the second derivative $d^2\theta/d\sigma^2$ with respect to strain. To facilitate derivative calculations and reduce noise in the experimental data, ninth-order polynomial fitting was performed on each stress–strain curve using Origin 2019, with coefficients of determination (R^2) exceeding 0.99. This allowed smooth evaluation of the first, second, and third derivatives for the critical strain analysis. In addition, nonlinear fitting was employed for modeling dynamic recrystallization kinetics from recrystallized fraction versus time data, again yielding R^2 values close to unity.

Overall, the same methodology established in [12] was applied here, ensuring consistency while allowing direct comparison of the Ti- and Nb-containing steels with the baseline boron steel.

3. Result and discussion

Strain–Stress Flow Curves

To analyze the hot deformation and recrystallization behavior, the corrected stress–strain flow curves were evaluated at different deformation temperatures and strain rates.

In our previous work the flow curves of FB are presented. the alloy shows typical high-temperature deformation characteristics. At lower temperatures and higher strain rates (850 °C at 10 s^{-1} and 1 s^{-1}), the curves display a continuous increase in stress without a distinct peak, indicating that dynamic recovery (DRV) dominates. With decreasing strain rate and increasing temperature, peak stress becomes progressively more evident, reflecting the onset of dynamic recrystallization (DRX). For example, at 850 °C a peak appeared only at 0.1 s^{-1}, while at 950 °C peaks were present at all strain rates except 10 s^{-1}. At 1050 and 1150 °C, clear DRX peaks were observed under all deformation conditions. These trends are consistent with the requirement of sufficient thermomechanical energy for nucleation and growth of DRX grains. At high strain rates and low temperatures, dislocation generation outpaces recovery and diffusion, thereby suppressing DRX.

The flow curves of the FBT are shown in Figure 3. The general trend with temperature and strain rate is similar to FB, namely, stress levels decrease with higher temperatures and lower strain rates. However, the absolute stress levels of FBT are consistently higher than those of

[DOI: 10.22068/ijmse.4448]

FB. More importantly, the DRX activity appears significantly reduced in FBT: at 850 °C only the 0.01 s^{-1} curve shows a weak peak, while at higher temperatures peak strains shift to larger values, and at 1150 °C peaks are observed across all conditions. This trend is consistent with the established mechanism in the literature, where the pinning effect of TiN precipitates on dislocation motion and grain boundary migration, which retards DRX [4]. The subsequent microstructural analysis of the FBT alloy (Section 3.5), which reveals Ti-rich precipitates and a significantly refined grain structure supports this interpretation and provides direct evidence for the operative retardation mechanism in the present study.

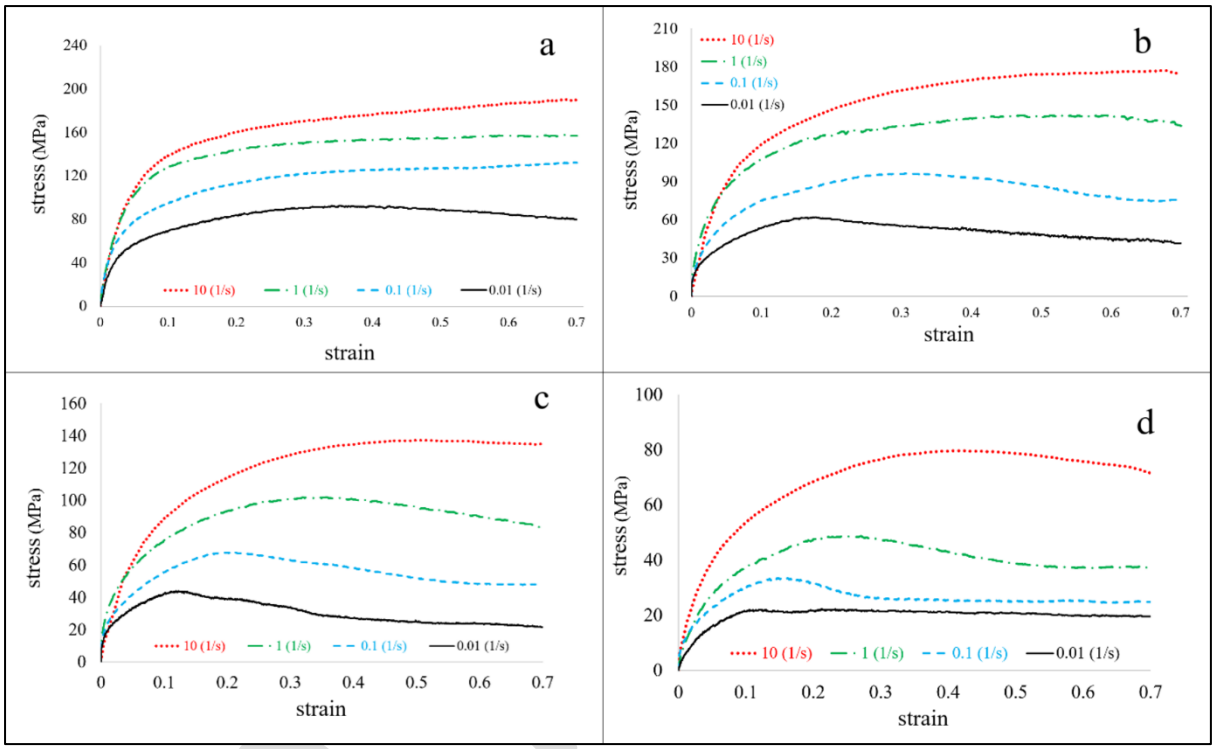

Figure 3. Flow curves of the FBT sample at different temperatures: a) 850 °C, b) 950 °C, c) 1050 °C, and d) 1150 °C.

For the FBN, the flow curves in Figure 4 also reveal notable differences. Similar to FBT, the stress levels are higher than FB across all conditions, and in some cases higher than FBT. At 10 s^{-1} strain rate, no peaks are observed regardless of temperature, indicating DRV-dominated behavior. Even at elevated temperatures, the peak stresses occur at relatively large strains, suggesting delayed DRX. Compared with FB, the FBN alloy demonstrates increased strength which may occur due to finer microstructure, and restricted recrystallization activity particularly at lower temperatures. This mechanical response is consistent with the widely reported mechanism wherein Nb(C,N) precipitates strongly interact with dislocations and grain boundaries, thereby retarding recrystallization [4] [5]. This interpretation is supported by our experimental findings for the FBN alloy: the significant increase in deformation activation energy, the marked delay in critical and peak strains, and the microstructural evidence of refined grains alongside Nb-containing precipitates at phase interfaces.

[DOI: 10.22068/ijmse.4448]

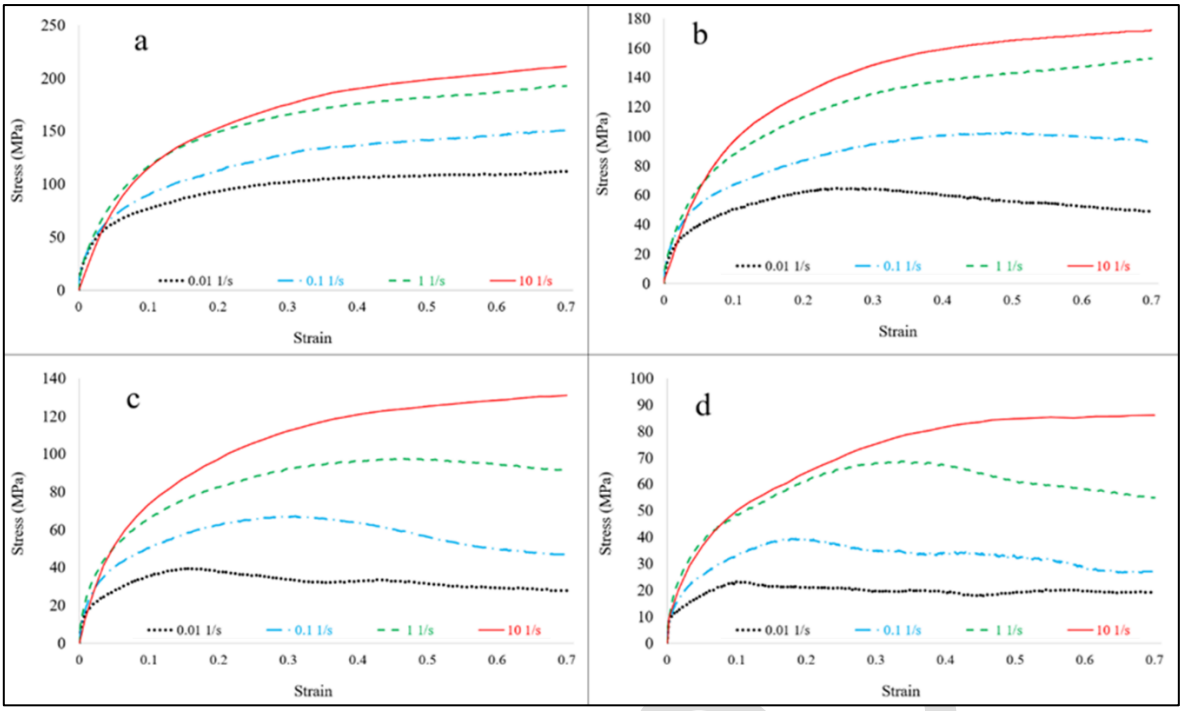

Figure 4. Flow curves of the FBN sample at different temperatures: a) 850 °C, b) 950 °C, c) 1050 °C, and d) 1150 °C.

Overall, these initial flow curve observations show that while FB exhibits clear DRX at high temperatures and low strain rates, the addition of Ti and Nb increases the flow stress levels and suppresses DRX kinetics. This trend is examined more quantitatively in the following sections through constitutive modeling and kinetic analysis.

Arrhenius Relations and Constitutive Equations

It should be noted that the methodology, equations, and calculation procedures presented in this section were previously established in our previous work for FB steel. They are included here primarily for clarification purposes and to provide a consistent basis for comparison with the Ti- and Nb-containing alloys (FBT and FBN).

To investigate the relationship between the stress–strain curves and the key thermomechanical process parameters, namely deformation temperature and strain rate, the Zener–Hollomon parameter was employed, expressed as [12]:

$$Z = \dot{\varepsilon} \exp\left(\frac{Q}{RT}\right) \quad (1)$$

where Q is the activation energy for deformation, T is the deformation temperature, and R is the universal gas constant. According to this relationship, a decrease in strain rate or an increase in deformation temperature corresponds to a reduction in the Zener–Hollomon parameter Z, while an increase in strain rate or decrease in temperature results in a higher Z value.

[DOI: 10.22068/ijmse.4448]

To describe the relationship between Z and the flow stress of the material, different functional forms can be applied depending on the stress and strain conditions. These include the power-law relation for low stress/strain, the exponential relation for high stress/strain, and the hyperbolic sine relation which accurately models the flow behavior under all stress and strain conditions [12]:

$$Z = A\,\sigma^{n'} \qquad \text{(Low } \varepsilon \text{ \& } \sigma\text{)} \qquad (2)$$

$$Z = B\exp(\beta\sigma) \qquad \text{(High } \varepsilon \text{ \& } \sigma\text{)} \qquad (3)$$

$$Z = C\,[\sinh(\alpha\sigma)]^{n} \qquad \text{(Any } \varepsilon \text{ \& } \sigma\text{)} \qquad (4)$$

where A, B, C, n′, β, n, and α are material constants. By combining Equations 1 to 4 and applying natural logarithms, the general expressions describing the simultaneous effects of stress, strain rate, and temperature are obtained:

$$\ln\dot{\varepsilon} = \ln A + n'\ln\sigma - \frac{Q_1}{RT} \qquad \text{(Low } \varepsilon \text{ \& } \sigma\text{)} \qquad (5)$$

$$\ln\dot{\varepsilon} = \ln B + \beta\sigma - \frac{Q_2}{RT} \qquad \text{(High } \varepsilon \text{ \& } \sigma\text{)} \qquad (6)$$

$$\ln\dot{\varepsilon} = \ln C + n\ln[\sinh(\alpha\sigma)] - \frac{Q_3}{RT} \qquad \text{(Any } \varepsilon \text{ \& } \sigma\text{)} \qquad (7)$$

The constants are determined as follows:

$$n' = \left(\frac{\partial\ln\dot{\varepsilon}}{\partial\ln\sigma}\right)_{\varepsilon,T} \qquad (8)$$

$$\beta = \left(\frac{\partial\ln\dot{\varepsilon}}{\partial\ln\sigma}\right)_{\varepsilon,T} \qquad (9)$$

$$n = \left(\frac{\partial\ln\dot{\varepsilon}}{\partial\ln[\sinh(\alpha\sigma)]}\right)_{\varepsilon,T} \qquad (10)$$

$$Q_1 = \left(\frac{\partial\ln\sigma}{\partial(\frac{1}{T})}\right)_{\varepsilon,\dot{\varepsilon}} \qquad (11)$$

$$Q_2 = \left(\frac{\partial\sigma}{\partial(\frac{1}{T})}\right)_{\varepsilon,\dot{\varepsilon}} \qquad (12)$$

$$Q_3 = \left(\frac{\partial\ln[\sinh(\alpha\sigma)]}{\partial(\frac{1}{T})}\right)_{\varepsilon,\dot{\varepsilon}} \qquad (13)$$

For these calculations, stress values corresponding to 0.2 and 0.6 strains were extracted from the experimental stress–strain curves in Figures 5 and 6 for FBT and FBN respectively. Figures 5(a–c) and 6(a–c) show the linear fits for n′, β, and n at each deformation temperature for all three alloys. The average slopes of these lines yield the corresponding material constants.

[DOI: 10.22068/ijmse.4448]

The stress coefficient α is then calculated as α=β/n′ [28] and used in determining n in Equation 7. Similarly, Figure 5(d-f) and Figure 6(d-f) illustrate the determination of activation energies Q1, Q2, and Q3 for FBT, and FBN, respectively, with averages of the slopes providing the final Q values.

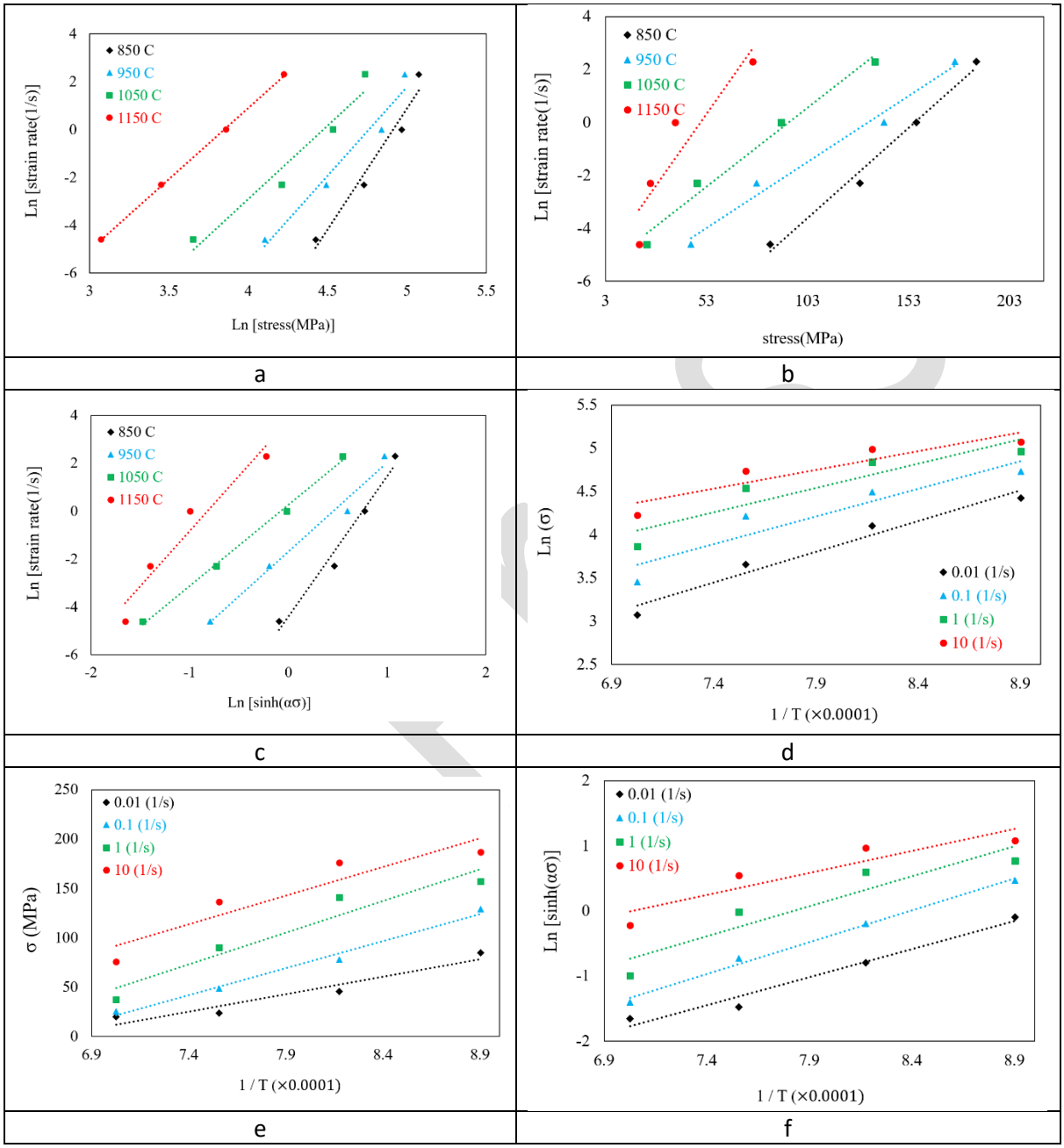

Figure 5. Arrhenius-type plots for the FBT sample: natural logarithm of a) power, b) exponential, and c) hyperbolic sine functions vs. strain rate, and d-f) their relations with inverse absolute temperature at different conditions.

[DOI: 10.22068/ijmse.4448]

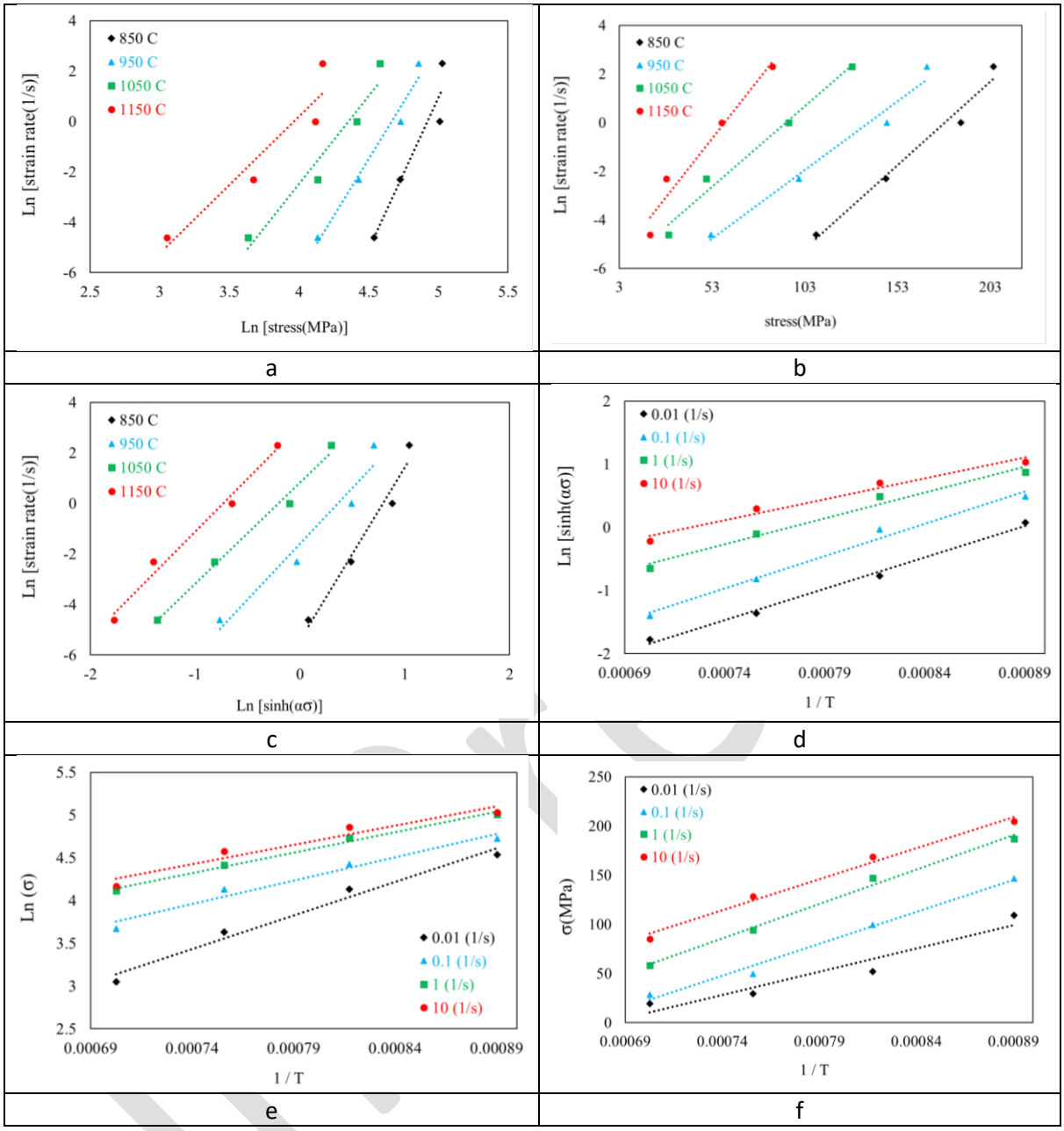

Figure 6. Arrhenius-type plots for the FBN sample: natural logarithm of a) power, b) exponential, and c) hyperbolic sine functions vs. strain rate, and d-f) their relations with inverse absolute temperature at different conditions.

The final material constants A, B, and C are obtained by adding Q/RT to the intercept of the corresponding plots and performing the required calculations. All constants are summarized in Table3 for FB, FBT, and FBN. To validate the accuracy of these constants, they were substituted back into Equations 2 to 4, and the Zener–Hollomon parameter was recalculated for each temperature and strain rate. Logarithmic plots of the predicted versus experimental data are presented in Figures 7 and 8, with linear fits showing high correlation coefficients (R^2).

[DOI: 10.22068/ijmse.4448]

Table 3. Constants obtained from Arrhenius relations (FB from [12]).

constant	value			strain
	FB	FBT	FBN	
n'	6.882	7.403	8.374	0.2
β	0.071	0.071	0.072	0.6
α	0.010	0.009	0.009	0.2 & 0.6
n	4.359	4.396	4.857	0.6
A	0.037	1.356	0.307	0.2
B	4.84×10^{9}	7.53×10^{9}	4.53×10^{11}	0.6
C	3.67×10^{11}	46.30×10^{11}	1.41×10^{14}	0.6
Q1 (KJ / mol)	313.21	315.61	368.77	0.2
Q2 (KJ / mol)	299.18	361.31	393.29	0.6
Q3 (KJ / mol)	293.37	314.15	353.04	0.6

Consistent with our previous work, the hyperbolic sine relation provides the most accurate modeling of the flow behavior for FBT and FBN, across both low (0.2) and high (0.6) strains. Accordingly, the estimated activation energies for FB, FBT, and FBN are 293.37 kJ/mol, 314.15 kJ/mol, and 353.04 kJ/mol, respectively. These results indicate that the addition of Ti and Nb significantly increases the activation energy for hot deformation, with Nb having the strongest effect due to the formation of stable Nb(C,N) precipitates that hinder dislocation motion and grain boundary migration [4] [5]. Finally, using the determined constants and equation 7, the constitutive equations for the FB [12], FBT and FBN alloys were established respectively as:

$$\ln Z = \ln \dot{\varepsilon} + \frac{293370}{8.314 \times T} = 26.63 + 4.359 \times \sinh(0.010\sigma) \quad (14)$$

$$\ln Z = \ln \dot{\varepsilon} + \frac{314150}{8.314 \times T} = 29.16 + 4.396 \times \sinh(0.009\sigma) \quad (15)$$

$$\ln Z = \ln \dot{\varepsilon} + \frac{353042}{8.314 \times T} = 32.58 + 4.858 \times \sinh(0.009\sigma) \quad (16)$$

These constitutive equations provide a quantitative basis for predicting the hot deformation behavior of all three alloys and allow for direct comparison of the effects of Ti and Nb additions relative to the base FB steel.

[DOI: 10.22068/ijmse.4448]

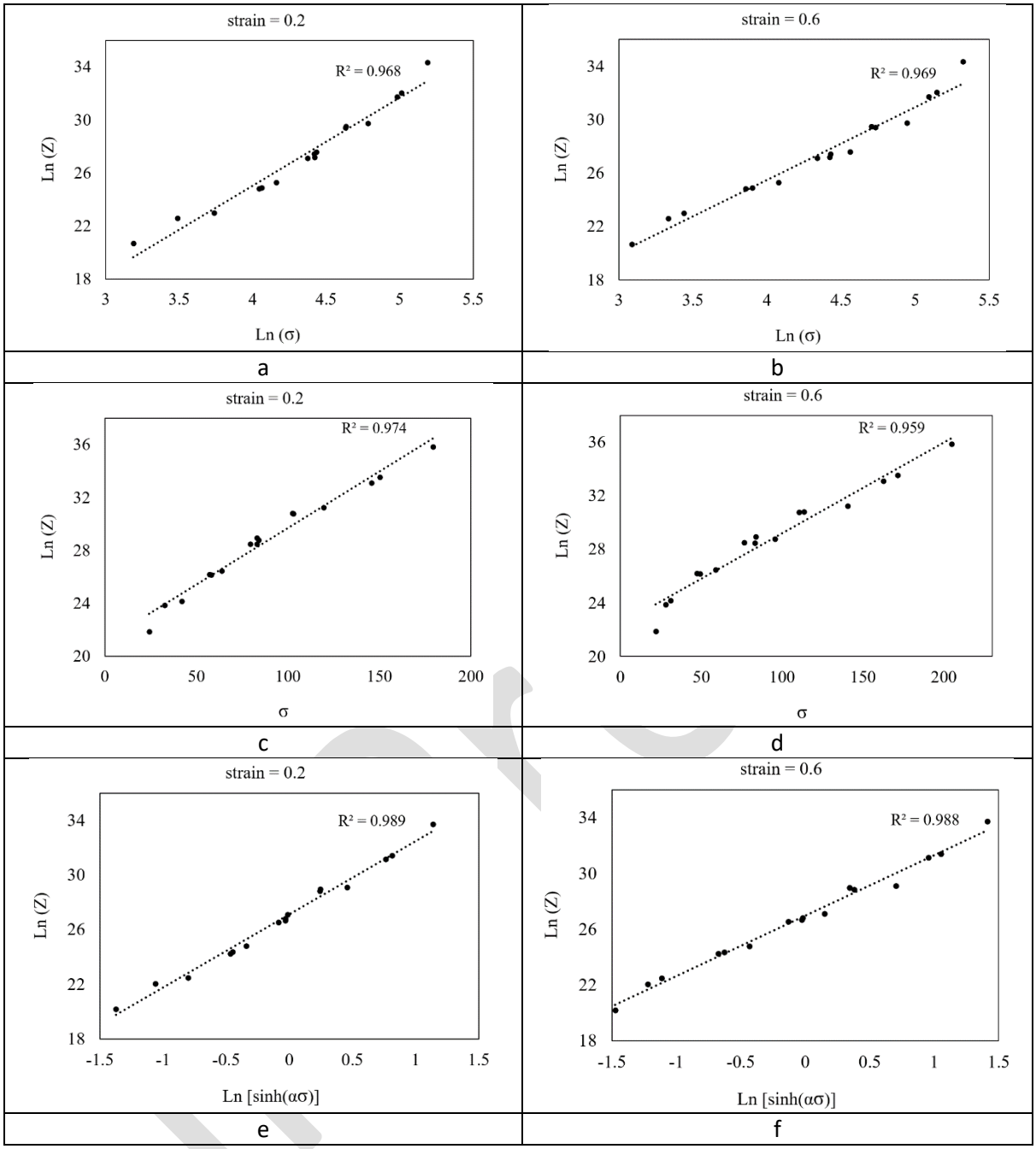

Figure 7. Arrhenius relationships vs Z values for the FBT sample at strains of 0.2 and 0.6: (a, b) power-law relationship; (c, d) exponential relationship; (e, f) hyperbolic sine relationship.

According to the calculations, the activation energy differs among the three alloys, with FBT and FBN exhibiting higher deformation activation energies than FB, reflecting the effects of Ti and Nb additions observed in the previous sections. The higher flow stress and strength levels in FBT, caused by microstructural changes induced by Ti, contribute to this increase, while in FBN, the even stronger interaction of Nb(C,N) precipitates with dislocations and grain boundaries further raises the activation energy. These differences are consistent with the qualitative and quantitative trends previously discussed for all three alloys.

[DOI: 10.22068/ijmse.4448]

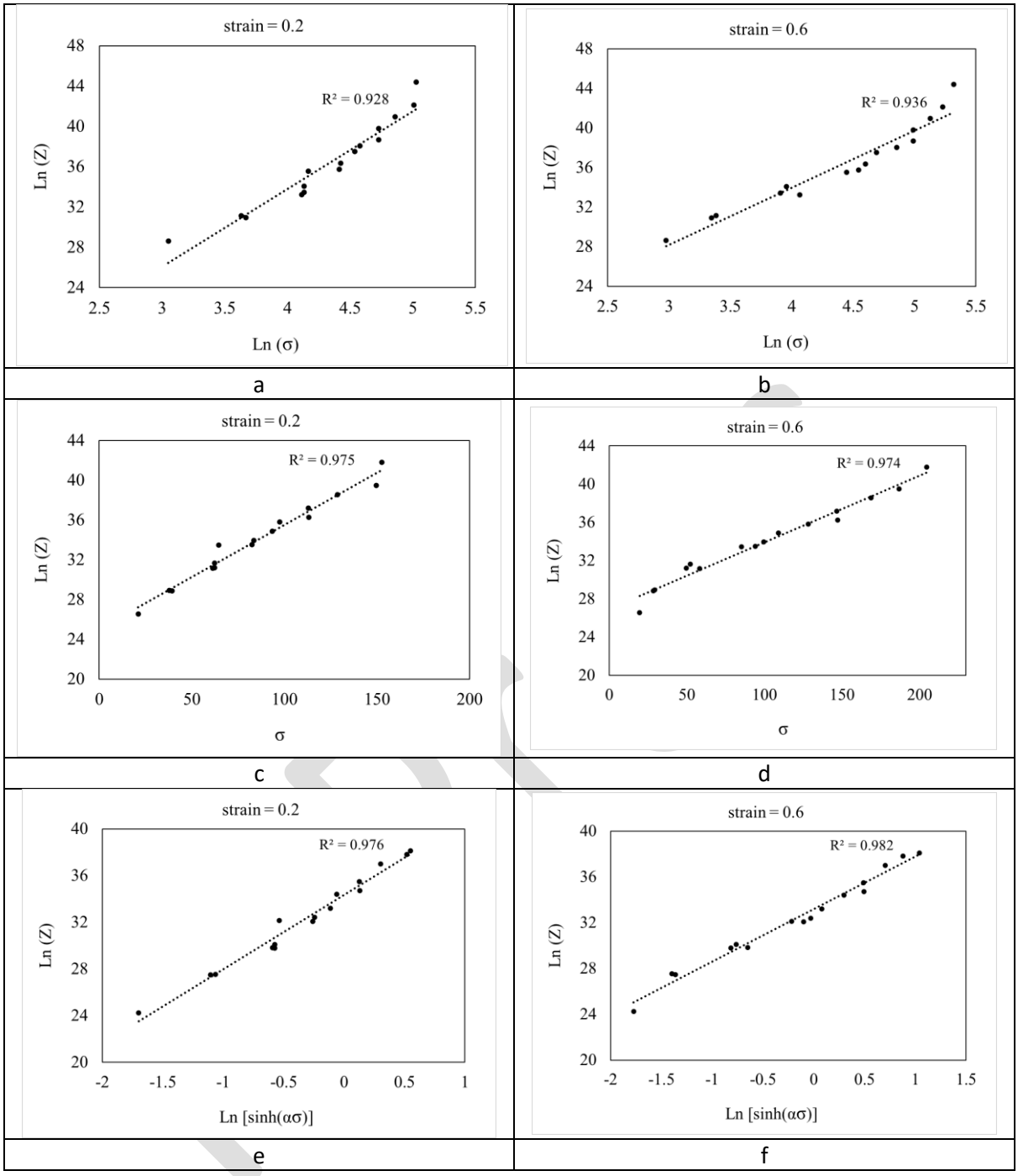

Figure 8. Arrhenius relationships vs Z values for the FBN sample at strains of 0.2 and 0.6: (a, b) power-law relationship; (c, d) exponential relationship; (e, f) hyperbolic sine relationship.

Overall, the effect of boron on the hot deformation behavior of low-carbon steels depends strongly on chemical composition and the presence of other alloying elements, and in the case of FBN, the combined influence of Nb and B further increases activation energy and modifies DRX kinetics compared with FB and FBT.

During high-temperature deformation, the onset of dynamic recrystallization (DRX) occurs at a strain lower than the peak strain, referred to as the critical strain (ε_c). By applying stress as a

[DOI: 10.22068/ijmse.4448]

function of strain and finding its root, εc is obtained. Due to the presence of the first derivative in the denominator, a vertical asymptote appears in the diagram, which corresponds to the peak strain (ε_p). Other characteristic values such as the critical stress (σ_c), peak stress (σ_p), saturation stress (σ_s), and steady-state stress (σ_{ss}) were also determined in this. This methodology and its basis have been described in detail in our previous work, and they are reproduced here mainly for clarity and to allow a consistent comparison among the three alloys (FB, FBT, and FBN).

The calculated characteristic stresses and strains for all hot compression tests of FB, FBT, and FBN are presented in Table 4. In some cases, σp and σss could not be identified within the applied strain range due to either the absence of DRX at the tested temperature or the possibility of their occurrence at higher strains beyond the experimental limit. Overall, the trends show that increasing strain rate and decreasing temperature shift all characteristic values (ε_c, ε_p, σ_c, σ_p, σ_s, and σ_{ss}) to higher levels. Comparison among the alloys reveals that FBT exhibits higher critical and peak values than FB, which reflects the strengthening and delayed DRX behavior caused by Ti addition. Furthermore, FBN shows the highest characteristic stresses and most delayed critical strains among all three steels, consistent with the strong interaction of Nb(C,N) precipitates with dislocations and grain boundaries. Thus, the ranking of characteristic parameters are fully consistent with the earlier observations of flow behavior and activation energy analysis.

By comparing the data in Tables 4, it is observed that with increasing temperature and decreasing strain rate, the values of critical strain and stress (ε_c, σ_c) as well as peak strain and stress (ε_p, σ_p) follow a decreasing trend. This behavior can be correlated with the Zener–Hollomon parameter, which provides a unified description of the effects of temperature and strain rate. Using Equation 1 together with the activation energy values obtained in the previous section, the natural logarithm of Z was plotted against the natural logarithm of the critical and peak stresses and strains. The results for FBT and FBN are shown in Figures 9 and 10, where linear fits to the data are also presented.

Based on these plots, the relationships between Z and the characteristic parameters were determined. For FBT, the corresponding equations are shown in Equations 17 to 20, and finally for FBN, the fitted equations are provided in Equations 21 to 24. A comparison among the three steels reveals that while all alloys show similar functional dependence on Z, the coefficients shift to higher values when moving from FB and FBT to FBN. This indicates that the addition of Nb increases the characteristic stresses and delays DRX initiation compared to FB and FBT.

[DOI: 10.22068/ijmse.4448]

Table 4. Characteristic strains and stresses of the FB, FBT and FBN sample at different temperatures and strain rates. (FB from [12])

T (°C)	$\dot{\varepsilon}$ (s^{-1})	ε_c			σ_c (MPa)			ε_p			σ_p (MPa)			σ_{ss} (MPa)			σ_s (MPa)		
		fb	fbt	fbn	fb	fbt	fbn	fb	fbt	fbn	fb	fbt	fbn	fb	fbt	fbn	fb	fbt	fbn
850	10	0.343	0.185	0.646	195.3	157.7	219.1	-	-	-	-	-	-	-	-	-	217.2	188.0	240.3
	1	0.337	0.177	0.470	164.5	140.9	182.1	-	-	-	-	-	-	-	-	-	180.6	161.6	213.2
	0.1	0.152	0.142	0.273	111.8	103.9	124.3	0.599	-	-	140.7	-	-	-	-	-	162.8	145.9	156.0
	0.01	0.140	0.140	0.343	75.2	75.9	103.5	0.371	0.371	-	90.9	91.7	-	-	-	-	132.4	128.9	115.4
950	10	0.342	0.372	0.623	158.0	167.8	170.7	0.628	0.661	-	162.8	176.9	-	-	-	-	169.3	183.5	278.8
	1	0.328	0.347	0.487	115.1	136.8	141.3	0.451	0.522	-	120.0	141.6	-	111.9	-	-	132.4	145.2	172.2
	0.1	0.145	0.155	0.497	72.8	83.2	101.4	0.340	0.310	0.582	86.6	96.2	102.1	74.3	75.0	-	120.6	140.1	103.3
	0.01	0.102	0.099	0.122	49.5	53.5	52.0	0.196	0.173	0.273	57.6	61.7	63.2	47.0	40.2	49.5	81.1	84.9	89.1
1050	10	0.176	0.210	0.535	99.7	116.0	123.7	0.395	0.516	-	113.5	137.1	-	110.5	-	-	127.6	158.5	185.0
	1	0.167	0.157	0.323	78.7	87.2	90.3	0.385	0.346	0.470	91.5	101.6	95.0	80.8	-	91.3	103.6	114.5	104.5
	0.1	0.103	0.097	0.125	49.1	54.7	52.2	0.224	0.205	0.304	58.5	67.6	64.5	48.8	48.1	47.1	73.5	98.7	98.0
	0.01	0.066	0.077	0.079	24.9	38.6	31.6	0.139	0.124	0.160	35.1	43.6	38.1	32.5	21.5	31.7	61.6	60.2	59.5
1150	10	0.179	0.178	0.174	81.6	65.8	58.5	0.477	0.423	-	97.0	79.6	-	93.5	-	-	106.7	99.1	176.0
	1	0.145	0.123	0.151	58.6	40.1	54.0	0.303	0.250	0.338	67.3	48.6	65.8	57.2	37.3	54.7	79.7	69.2	64.3
	0.1	0.098	0.082	0.101	37.8	27.9	31.9	0.165	0.156	0.186	43.2	33.4	37.7	30.2	25.8	33.3	59.5	46.1	62.0
	0.01	0.073	0.062	0.054	22.7	15.8	19.2	0.110	0.117	0.107	25.3	21.8	22.1	21.8	21.0	19.4	36.1	30.6	31.0

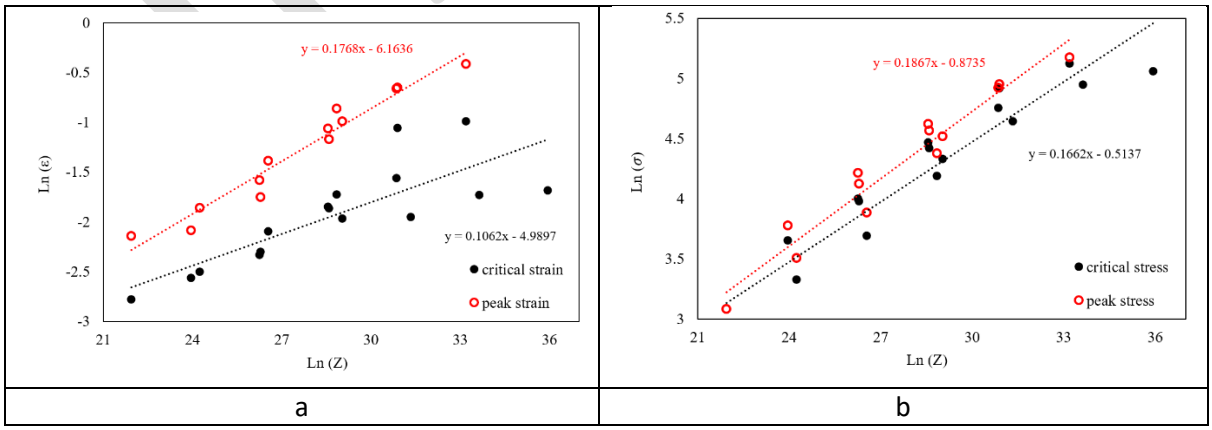

Figure 9. Relationship between the natural logarithm of the Z parameter and characteristic stress and strain values for the FBT sample: (a) critical and peak strains; (b) critical and peak stresses.

[DOI: 10.22068/ijmse.4448]

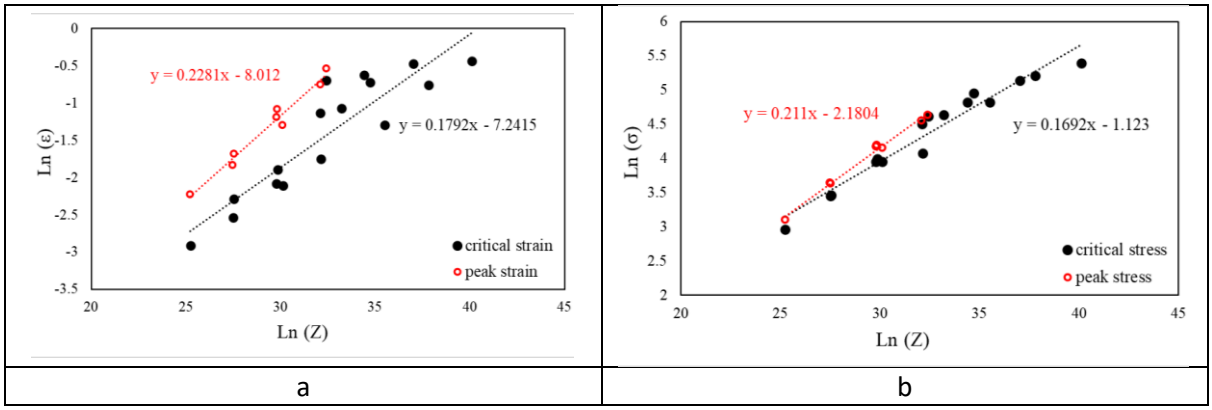

a b

Figure 10. Relationship between the natural logarithm of the Z parameter and characteristic stress and strain values for the FBT sample: (a) critical and peak strains; (b) critical and peak stresses.

$$\varepsilon_c = 6.81 \times 10^{-3} \times Z^{0.106} \quad (17)$$

$$\varepsilon_p = 2.10 \times 10^{-3} \times Z^{0.177} \quad (18)$$

$$\sigma_c = 5.98 \times 10^{-1} \times Z^{0.166} \quad (19)$$

$$\sigma_p = 4.17 \times 10^{-1} \times Z^{0.187} \quad (20)$$

$$\varepsilon_c = 7.16 \times 10^{-4} \times Z^{0.179} \quad (21)$$

$$\varepsilon_p = 3.31 \times 10^{-4} \times Z^{0.228} \quad (22)$$

$$\sigma_c = 3.25 \times 10^{-1} \times Z^{0.169} \quad (23)$$

$$\sigma_p = 1.13 \times 10^{-1} \times Z^{0.211} \quad (24)$$

Dynamic recrystallization modeling

The methodology for evaluating DRX kinetics through separation of the experimental flow stress curve into a dynamic recovery component and the actual measured stress has already been fully described in our previous work [12]. In short, the hypothetical dynamic recovery curve (σ_{WH}) can be expressed as:

$$\sigma_{WH} = [\sigma_s{}^2 + (\sigma_1{}^2 - \sigma_s{}^2)\exp(-k_2\Delta\varepsilon)]^{0.5} \quad (25)$$

where σ_s is the saturation stress, $\sigma 1$ is the stress before the critical point, k2 is the recovery constant, and $\Delta\varepsilon$ is the strain increment beyond the reference point. The DRX fraction is then obtained by comparing the experimental flow stress and the recovery curve:

[DOI: 10.22068/ijmse.4448]

$$X_{drx} = \frac{\sigma_{WH} - \sigma}{\sigma_s - \sigma_{ss}} \quad (26)$$

with σ_{ss} being the steady-state stress. The strain dependence of DRX evolution is finally quantified by the Avrami relationship:

$$X_{drx} = 1 - \exp\left(-k\left[\frac{\varepsilon - \varepsilon_c}{\dot{\varepsilon}}\right]^{n_A}\right) \quad (27)$$

where εc is the critical strain, k is the kinetic constant, and n_A is the Avrami exponent.

Figures 11 show the experimental DRX fractions and Avrami-type model predictions for FBT and FBN alloys under different hot deformation conditions. The fitting results confirm that the Avrami model accurately describes the recrystallization behavior across all alloys. In FB, DRX initiates earlier and reaches higher fractions, reflecting the relatively unhindered mobility of dislocations and limited solute drag. In contrast, both FBT and FBN display a clear delay in DRX initiation and reduced final fractions, consistent with the pinning effects of Ti- and Nb-related precipitates. Increasing deformation temperature enhances recovery and facilitates dislocation annihilation, raising the DRX fraction, while higher strain rates accelerate dislocation accumulation but suppress the final recrystallized volume, a trend observed in all three alloys.

Comparative analysis of the Avrami exponent (n_A) further highlights the different kinetics: FB shows the highest value (n_A = 2.09), confirming its rapid and more complete DRX process. FBT exhibits the lowest value (n_A = 1.65), indicating that Ti additions strongly restrict DRX due to solute–precipitate interactions and grain boundary pinning. FBN lies between the two (n_A = 1.88), but still below FB, consistent with the strong pinning effect of Nb-based precipitates such as NbC and Nb(C,N), which are well-documented in the literature to retard nucleation and growth of recrystallized grains. According to reported research, n_A typically ranges between 0.5 and 4 and is independent of transformation temperature but highly dependent on the nucleation mechanism of DRX. By increasing n_A from 0.5 to 4, the nucleation mechanism gradually shifts from instantaneous to continuous, while grain growth transitions from one-dimensional to two- and three-dimensional modes [29] [30].

Microstructural Investigation

First, the thermodynamic predictions of JMatPro were used to estimate the types and amounts of precipitates expected in the FBT and FBN samples. Figure 12 and 13 shows the predicted precipitates in the FBT and FBN samples respectively. Comparing this with the FB sample indicates that the addition of Ti leads to the suppression of BN precipitates and the formation of TiN. This occurs because titanium has a higher affinity for nitrogen than boron and forms TiN at higher temperatures than BN, preventing boron from reacting with nitrogen. The presence of Ti also modifies the amount and distribution of other precipitates. Equilibrium calculations suggest that approximately 13 ppm of boron remains in solid solution under these

[DOI: 10.22068/ijmse.4448]

conditions. Additionally, the presence of Nb in the FBN composition allows the formation of Nb(C,N), which can influence the material properties.

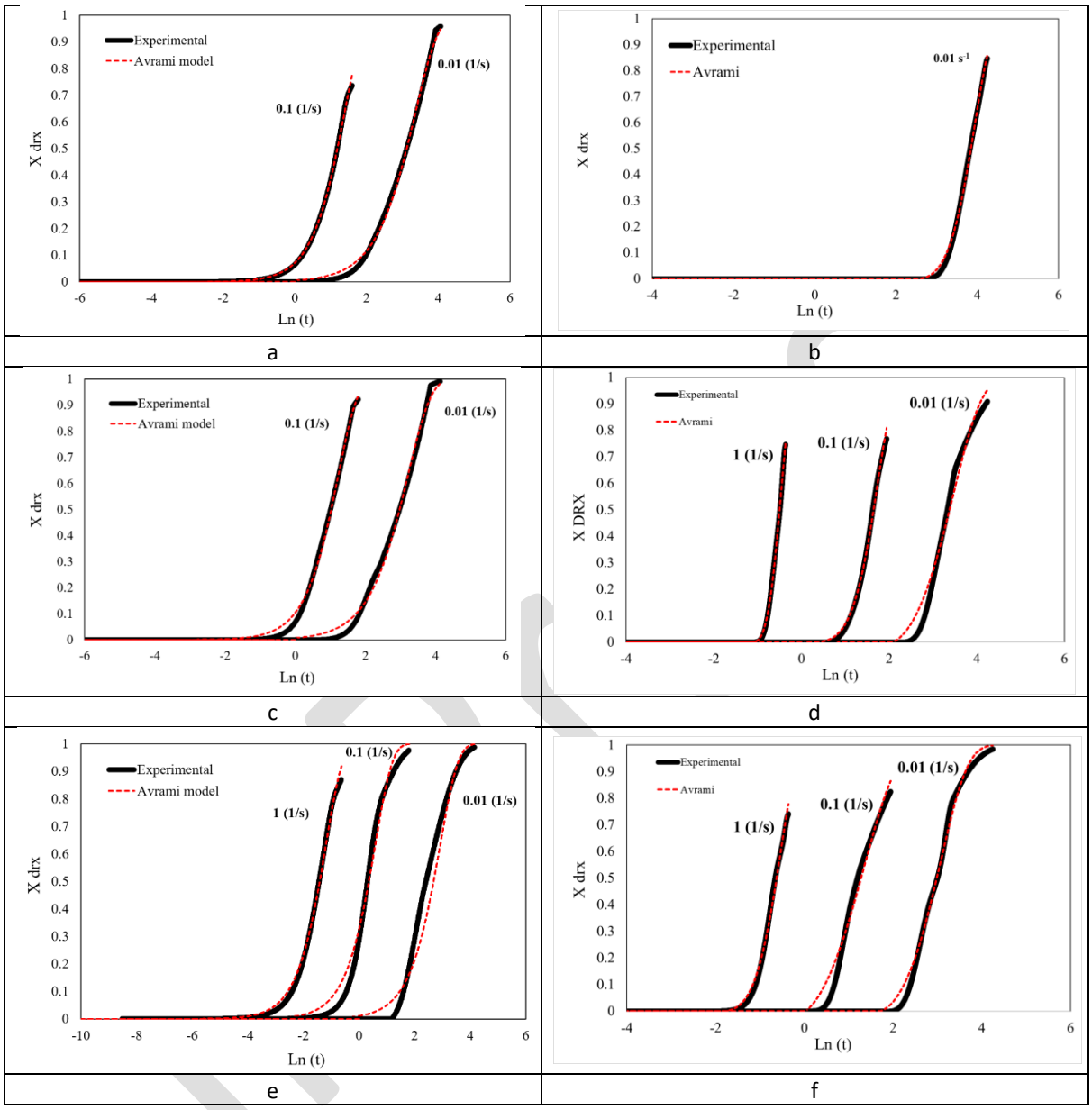

Figure 11. Xdrx fraction curves and Avrami model fits for FBT and FBN samples at different temperatures: (a, c, e) FBT at 950, 1050, and 1150 °C; (b, d, f) FBN at 950, 1050, and 1150 °C.

[DOI: 10.22068/ijmse.4448]

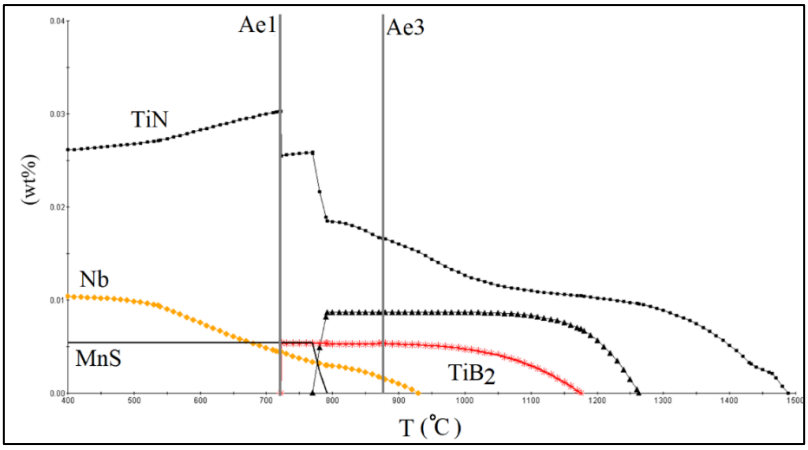

Figure 12. Thermodynamic analysis of the possible precipitates formed in the FBT sample.

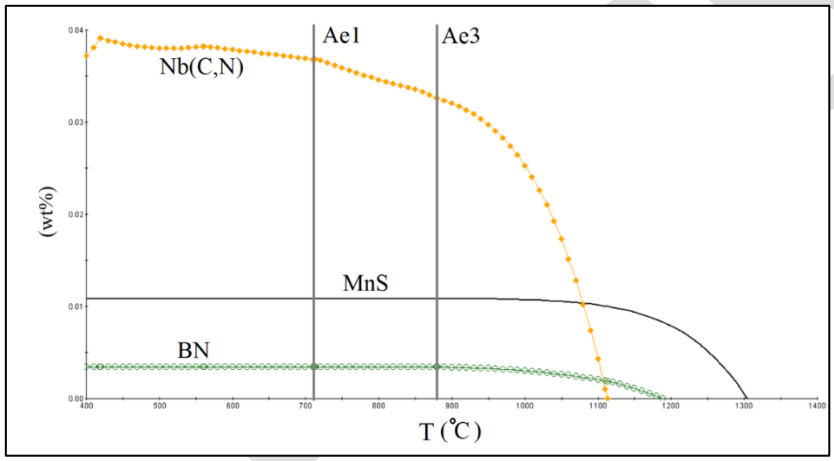

Figure 13. Thermodynamic analysis of the possible precipitates formed in the FBN sample.

While the microstructural investigation by SEM and OM of the FB sample was presented in our previous work, the current investigation focuses on the microstructure of FBT and FBN alloys. Figure 14 shows the SEM results for FBT. As illustrated in Figure 14a, the microstructure primarily consists of ferrite in the matrix and pearlite (marked as phase A), with the lamellar structure and carbon content similar to FB. However, thermodynamic calculations result by JMatPro indicate a substantial increase in the total precipitate fraction. The estimated weight fractions of the main precipitates are: ~0.020 wt.% (MnS, AlN, Nb(C,N)) in FB [12]; ~0.041 wt.% (TiN, Nb(C,N), MnS) in FBT; and ~0.052 wt.% (Nb(C,N), MnS, BN) in FBN. This quantitative increase, particularly the dominant roles of TiN in FBT and Nb(C,N) in FBN, aligns with the observed microstructural evolution. These precipitates are distributed not only along the grain boundaries but also within the grains. The EDS analysis of the precipitates labeled B (Figure 14 c) indicates a composition of approximately 69% Fe, 20% C, and 11% B, consistent with boron carbides and cementite forming at the grain boundaries. Additionally, backscattered electron imaging at higher magnification reveals other precipitates (Figure 14b, indicated with arrows) whose EDS composition (Figure 14d) includes ~35% Ti, 26% N, 10% C, and 16% B, suggesting the formation of titanium nitrides, carbides, or carbonitrides. These observations confirm that the addition of Ti modifies both the formation and distribution of

[DOI: 10.22068/ijmse.4448]

other precipitates, including boron-containing phases, which is expected to influence the hot deformation and DRX behavior as discussed in Sections 3.3 and 3.4.

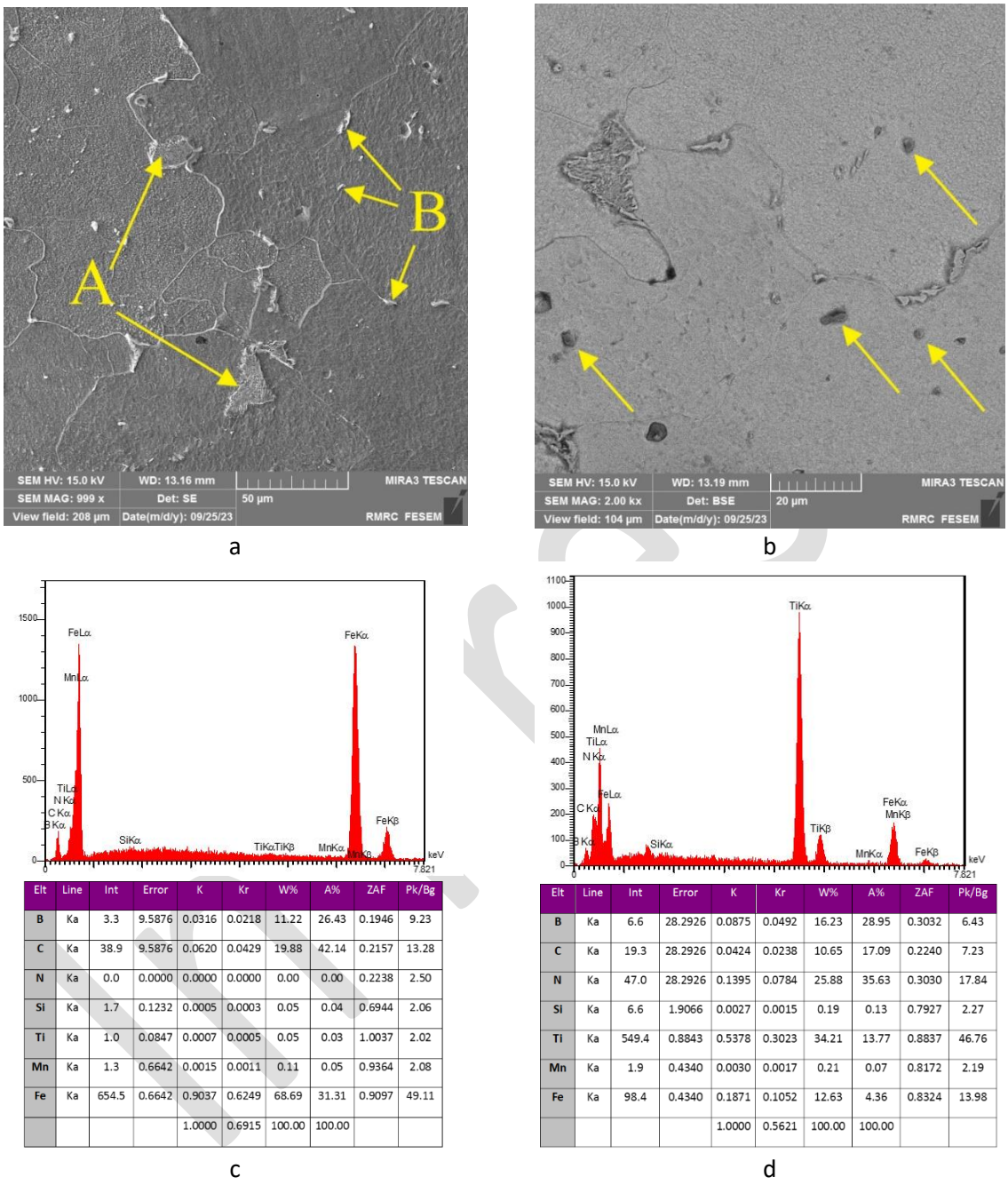

Elt	Line	Int	Error	K	Kr	W%	A%	ZAF	Pk/Bg
B	Ka	3.3	9.5876	0.0316	0.0218	11.22	26.43	0.1946	9.23
C	Ka	38.9	9.5876	0.0620	0.0429	19.88	42.14	0.2157	13.28
N	Ka	0.0	0.0000	0.0000	0.0000	0.00	0.00	0.2238	2.50
Si	Ka	1.7	0.1232	0.0005	0.0003	0.05	0.04	0.6944	2.06
Ti	Ka	1.0	0.0847	0.0007	0.0005	0.05	0.03	1.0037	2.02
Mn	Ka	1.3	0.6642	0.0015	0.0011	0.11	0.05	0.9364	2.08
Fe	Ka	654.5	0.6642	0.9037	0.6249	68.69	31.31	0.9097	49.11
				1.0000	0.6915	100.00	100.00		

c

Elt	Line	Int	Error	K	Kr	W%	A%	ZAF	Pk/Bg
B	Ka	6.6	28.2926	0.0875	0.0492	16.23	28.95	0.3032	6.43
C	Ka	19.3	28.2926	0.0424	0.0238	10.65	17.09	0.2240	7.23
N	Ka	47.0	28.2926	0.1395	0.0784	25.88	35.63	0.3030	17.84
Si	Ka	6.6	1.9066	0.0027	0.0015	0.19	0.13	0.7927	2.27
Ti	Ka	549.4	0.8843	0.5378	0.3023	34.21	13.77	0.8837	46.76
Mn	Ka	1.9	0.4340	0.0030	0.0017	0.21	0.07	0.8172	2.19
Fe	Ka	98.4	0.4340	0.1871	0.1052	12.63	4.36	0.8324	13.98
				1.0000	0.5621	100.00	100.00		

d

Figure 14. SEM analysis of the FBT sample: (a) SEM image of the microstructure, (b) SEM image of the microstructure in BSE mode, (c) EDS analysis of phase B, (d) EDS analysis of the precipitates shown in (b).

The SEM investigation of the FBN sample is shown in Figure 15. The microstructure consists of ferrite, pearlite, and precipitates at the grain boundaries, similar to the previous samples. The lamellar structure of phase A and its chemical composition remain consistent. Precipitates labeled B, analyzed by EDS (Figure 15c), contain ~77% Fe, 13% C, and 8% B, corresponding to boron carbides and cementite. As expected from the thermodynamic predictions, the addition

[DOI: 10.22068/ijmse.4448]

of Nb does not significantly alter the formation of boron-containing precipitates. Nb primarily contributes through the formation of Nb(C,N) precipitates, which are extremely fine and difficult to observe directly in SEM. Only backscattered electron imaging reveals distinct precipitates (Figure 15b, arrows), where brighter contrast at the edges indicates regions enriched with heavier elements. EDS analysis at these interfaces (Figure 15d) shows ~28% Mn, 13% S, 20% B, 22% C, and 1% Nb. This low Nb signal is consistent with the presence of fine Nb-enriched phases or solute clusters at the interface of the primary MnS and BN precipitates. Therefore, the conclusive identification of Nb(C,N) is supported by the convergence of thermodynamic calculation, which predicts its stability in the FBN composition, and the well-established literature [4] [5] [11] linking Nb additions to Nb(C,N) formation and strong DRX retardation, a behavior fully consistent with our experimental results for FBN (e.g., highest activation energy, most delayed critical strain). These SEM observations corroborate the material behavior described in previous sections: in FBT and FBN, the precipitate distribution and chemical interactions restrict dislocation mobility, reduce DRX activity, and increase critical stresses compared to FB, consistent with the trends discussed in Sections 3.3 and 3.4. Further high-resolution analyses would be required to fully resolve the fine Nb(C,N) precipitates and their exact influence on microstructural evolution.

In comparison to the results reported in our previous work for the FB alloy [12], the SEM analysis of the FBT and FBN samples revealed distinct differences in precipitate formation and distribution. In FBT, the addition of Ti altered the precipitation sequence, leading to the replacement of BN by TiN and Ti(C,N), with a higher overall precipitate fraction. These precipitates were distributed both along grain boundaries and within the grain interior, in contrast to FB where they were mainly concentrated at the boundaries. In FBN, however, the addition of Nb did not prevent the formation of BN, but it promoted the formation of Nb(C,N) phases, which were difficult to resolve under SEM due to their fine size. Nevertheless, some complex precipitates involving MnS and BN were detected. These microstructural modifications are directly linked to the differences in dynamic recrystallization behavior described earlier, where FBT and FBN showed delayed or less active DRX compared to FB.

The SEM-EDS analyses, alongside thermodynamic calculation by JmatPro and literature review, provide critical microstructural evidence that directly explains the distinct hot deformation behaviors of FBT and FBN compared to FB. In FBT, the suppression of BN and the formation of TiN/Ti(C,N) precipitates, distributed both intergranularly and intragranularly (Fig. 14), create a potent pinning network. These fine, thermally stable precipitates act as strong barriers to dislocation glide and climb during hot compression. Consequently, they effectively retard the annihilation and rearrangement of dislocations necessary for the onset of Dynamic Recovery (DRV) and, more importantly, for the nucleation of Dynamic Recrystallization (DRX). This pinning effect is the direct microstructural root cause of the observed increase in flow stress, elevated critical strain (εc), and the higher activation energy for deformation in FBT. In FBN, the retention of BN alongside the formation of ultra-fine Nb(C,N) precipitates (predicted thermodynamically and inferred from EDS at MnS interfaces) produces a different but equally effective strengthening mechanism. Nb(C,N) precipitates are renowned for their exceptional coherency strain fields and low solubility in austenite. Their interaction with

[DOI: 10.22068/ijmse.4448]

dislocations is not merely geometric pinning but also involves significant strain-field interactions, which dramatically increases the energy required for dislocation motion and grain boundary migration. This explains why FBN exhibited the highest flow stress, the most delayed DRX initiation (largest εc and εp), and the greatest activation energy (Q = 353.04 kJ/mol) among the three steels. Thus, the SEM-verified precipitate chemistry and distribution offer definitive proof for the mechanisms behind the constitutive and kinetic trends presented in Sections 3.2 and 3.3

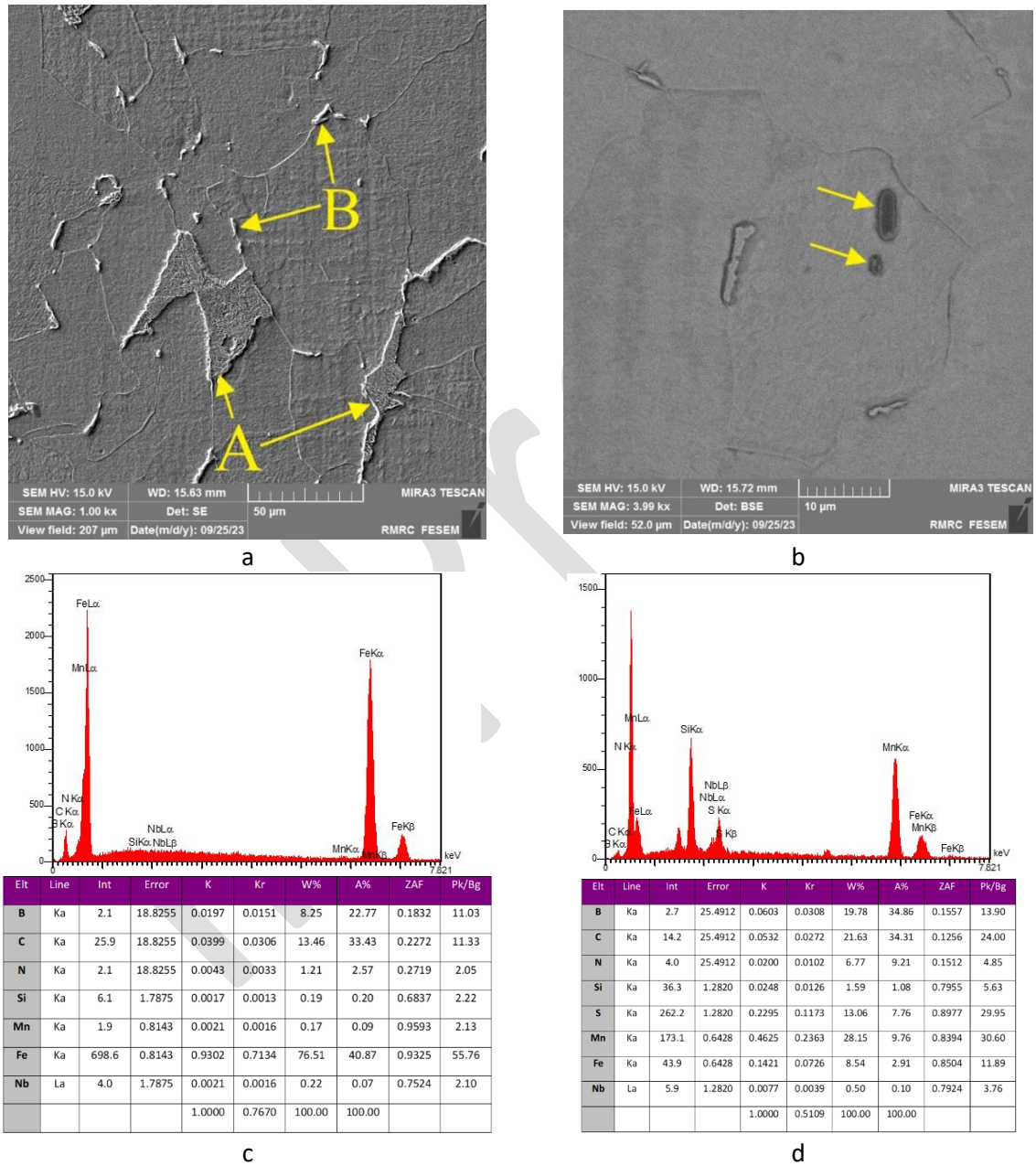

Elt	Line	Int	Error	K	Kr	W%	A%	ZAF	Pk/Bg
B	Ka	2.1	18.8255	0.0197	0.0151	8.25	22.77	0.1832	11.03
C	Ka	25.9	18.8255	0.0399	0.0306	13.46	33.43	0.2272	11.33
N	Ka	2.1	18.8255	0.0043	0.0033	1.21	2.57	0.2719	2.05
Si	Ka	6.1	1.7875	0.0017	0.0013	0.19	0.20	0.6837	2.22
Mn	Ka	1.9	0.8143	0.0021	0.0016	0.17	0.09	0.9593	2.13
Fe	Ka	698.6	0.8143	0.9302	0.7134	76.51	40.87	0.9325	55.76
Nb	La	4.0	1.7875	0.0021	0.0016	0.22	0.07	0.7524	2.10
				1.0000	0.7670	100.00	100.00		

Elt	Line	Int	Error	K	Kr	W%	A%	ZAF	Pk/Bg
B	Ka	2.7	25.4912	0.0603	0.0308	19.78	34.86	0.1557	13.90
C	Ka	14.2	25.4912	0.0532	0.0272	21.63	34.31	0.1256	24.00
N	Ka	4.0	25.4912	0.0200	0.0102	6.77	9.21	0.1512	4.85
Si	Ka	36.3	1.2820	0.0248	0.0126	1.59	1.08	0.7955	5.63
S	Ka	262.2	1.2820	0.2295	0.1173	13.06	7.76	0.8977	29.95
Mn	Ka	173.1	0.6428	0.4625	0.2363	28.15	9.76	0.8394	30.60
Fe	Ka	43.9	0.6428	0.1421	0.0726	8.54	2.91	0.8504	11.89
Nb	La	5.9	1.2820	0.0077	0.0039	0.50	0.10	0.7924	3.76
				1.0000	0.5109	100.00	100.00		

Figure 15. SEM analysis of the FBN sample: (a) SEM image of the microstructure, (b) SEM image of the microstructure in BSE mode, (c) EDS analysis of phase B, (d) EDS analysis of the precipitates shown in (b).

[DOI: 10.22068/ijmse.4448]

The optical microscopy results of hot-compressed samples further confirm these observations. The microstructures of FBT and FBN samples deformed at 950 and 1150 °C under strain rates of 0.1 s^{-1} and 1 s^{-1} are presented in Figure16, and analyzed using MIP software, with the corresponding grain size histograms presented in Figure 17. At 950°C, both alloys exhibited elongated and partially recrystallized grains with lower average grain size compared to FB, reflecting the inhibition of DRX by Ti- and Nb-containing precipitates. For FBT, the grains were notably elongated along the horizontal axis (perpendicular to the compression direction), with average grain sizes of 11.8 and 9.9 μm at 0.1 s^{-1} and 1 s^{-1}, respectively. Similarly, FBN showed jagged and irregular grain boundaries, with unusually shaped grains and average sizes of 11.0 and 9.5 μm for the same conditions. At 1150°C, both alloys showed more equiaxed grains, with averages of 17.3 and 15.5 μm for FBT and 17.0 and 15.6 μm for FBN at 0.1 s^{-1} and 1 s^{-1}, respectively. In both cases, higher strain rates produced thicker and clearer grain boundaries, whereas lower strain rates favored relatively coarser equiaxed grains.

The grain size distributions derived from histogram analysis confirmed that FBT and FBN samples exhibit a narrower and sharper peak around the average grain size compared to FB. This indicates a more uniform grain size distribution in these micro-alloyed steels, consistent with the retarded but more controlled recrystallization process caused by Ti and Nb-rich precipitates. In contrast, FB exhibited a wider distribution and larger average grain size under similar conditions, in agreement with its more active DRX behavior. Therefore, these microstructural observations strongly support the mechanical and kinetic results presented in Sections 3.3 and 3.4, demonstrating that Ti and Nb additions significantly refine and stabilize the grain structure by delaying recrystallization and limiting grain growth.

The quantitative analysis of grain size distributions in Fig. 17 reveals more about recrystallization behavior governed by Ti and Nb. While both FBT and FBN show significantly refined and more homogeneous grains compared to FB, a key difference exists between them. FBN consistently exhibits a narrower distribution peak (e.g., at 1150°C, 0.1 s^{-1}) than FBT. This superior uniformity in FBN can be attributed to the nature of Nb(C,N) precipitation. As a strong carbide/nitride former, Nb leads to a high number density of fine, Zener-pinning particles that exert a more uniform restraint on all grain boundaries during and after deformation. This results in a more synchronized and homogeneous suppression of grain growth, leading to a tighter grain size distribution. In contrast, the precipitate distribution in FBT, involving both TiN and residual boron-carbides, might be slightly less uniform in size and spacing, leading to a marginally broader distribution of grain sizes. This microstructural observation aligns perfectly with the Avrami kinetics (Section 3.4): the slightly higher Avrami exponent for FBN (nA=1.88) compared to FBT (nA=1.65) suggests a recrystallization process that, while still suppressed relative to FB, proceeds in a somewhat more progressive and spatially uniform manner. The finer and more uniform grain structure in both microalloyed steels, ultimately a result of controlled precipitate-driven pinning, is the direct microstructural manifestation of their delayed DRX kinetics and enhanced resistance to grain coarsening at high temperatures.

[DOI: 10.22068/ijmse.4448]

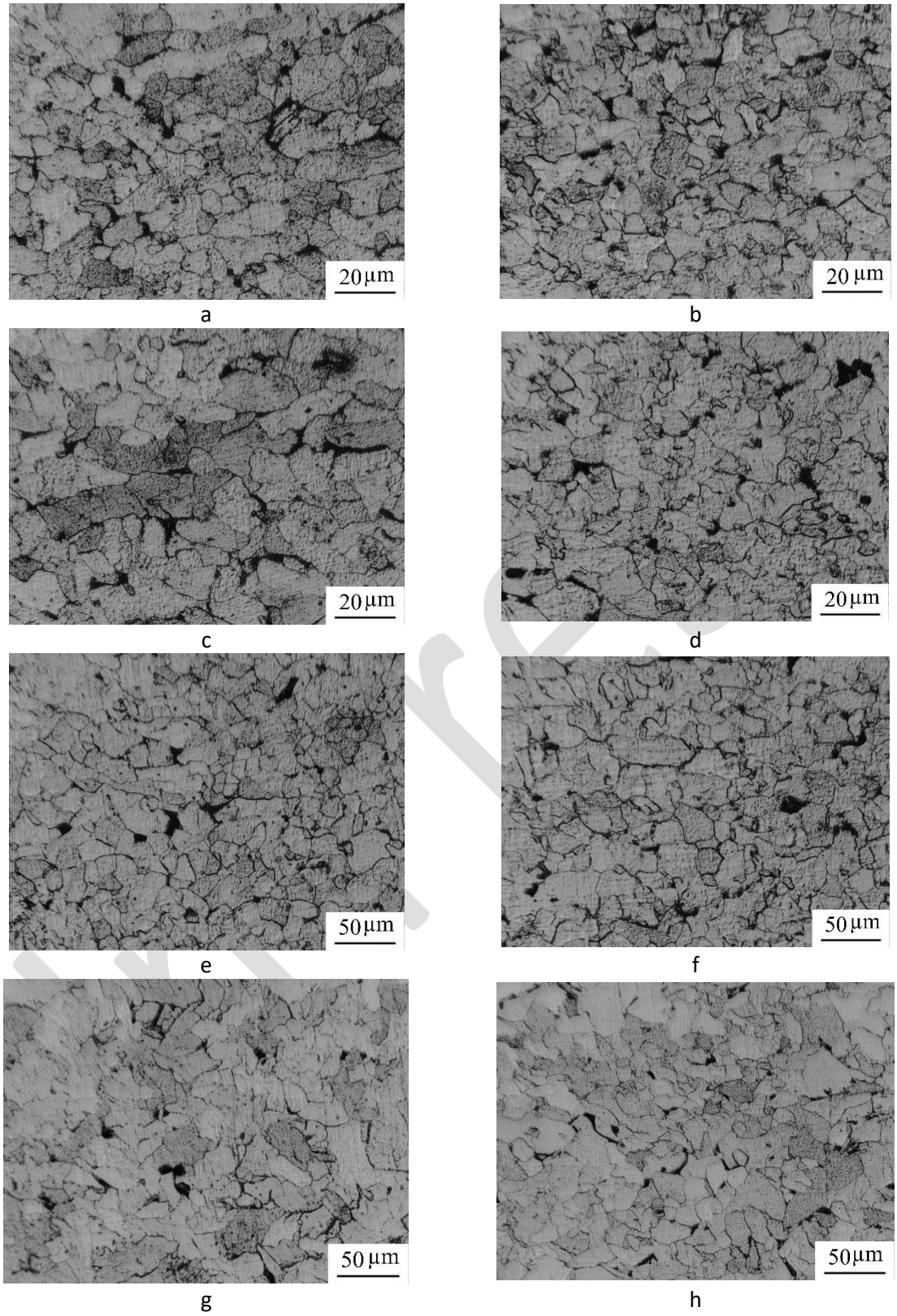

Figure 16. Microstructural images of FBT and FBN samples at different temperatures and strain rates respectively: (a, c, e, g) FBT at 950 °C (0.1, 1 s^{-1}) and 1150 °C (0.1, 1 s^{-1}); (b, d, f, h) FBN at 950 °C (0.1, 1 s^{-1}) and 1150 °C (0.1, 1 s^{-1}).

[DOI: 10.22068/ijmse.4448]

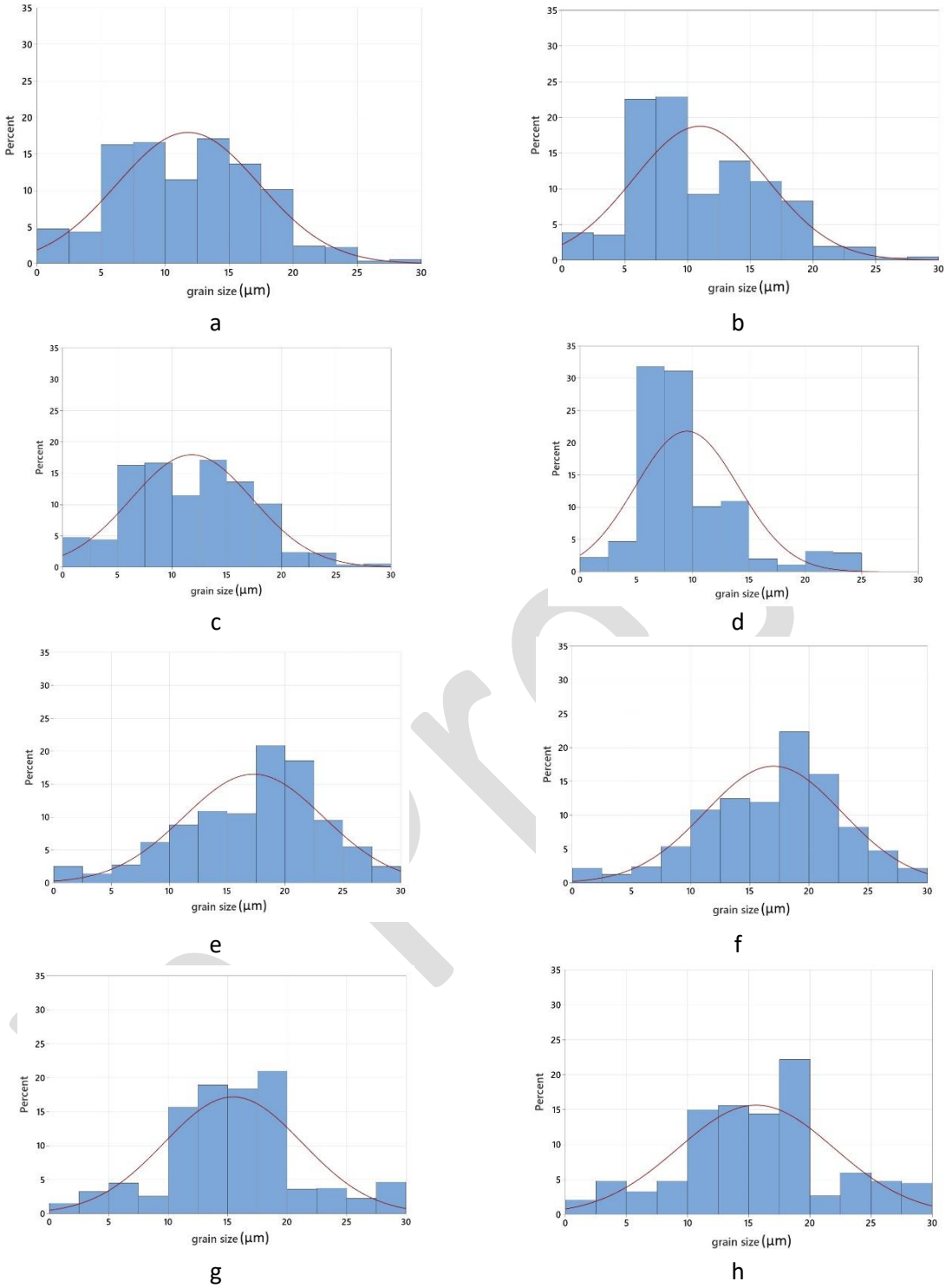

Figure 17. Grain size distribution analysis of FBT and FBN samples at different temperatures and strain rates respectively: (a, c, e, g) FBT at 950 °C (0.1, 1 s^{-1}) and 1150 °C (0.1, 1 s^{-1}); (b, d, f, h) FBN at 950 °C (0.1, 1 s^{-1}) and 1150 °C (0.1, 1 s^{-1}).

[DOI: 10.22068/ijmse.4448]

4. Conclusion

This study extended our previous work on boron-treated low-carbon steel (FB, [12]) by investigating the influence of Ti (FBT) and Nb (FBN) additions on hot deformation behavior, dynamic recrystallization, and microstructural evolution. In comparison with FB, both alloys exhibited notable changes in flow response, kinetic parameters, and grain refinement.

1 - The stress–strain curves of FBT and FBN consistently showed higher flow stresses and postponed DRX initiation relative to FB. The effect was more pronounced in FBN, where peak stresses shifted further and recrystallization was often suppressed under high strain rate conditions.

2 - Arrhenius analysis confirmed a progressive increase in deformation activation energy from 293.37 kJ/mol for FB to 314.15 kJ/mol for FBT and 353.04 kJ/mol for FBN. This trend demonstrates that Ti and Nb additions raise the energy barrier for plastic flow, with Nb exerting the strongest influence.

3 - The characteristic parameters (σ_c, σ_p, ε_c, ε_p) were consistently greater in FBT than in FB, while FBN exhibited the largest values overall, signifying delayed softening and higher resistance to recrystallization compared with the baseline alloy.

4 - Avrami modeling showed that FB had the highest exponent ($n_A = 2.09$), reflecting faster nucleation and growth of recrystallized grains. FBT displayed the lowest value (1.65), consistent with strong suppression of DRX by Ti(C,N) precipitates, while FBN lay between the two (1.88), though still below FB, indicating a slower but more progressive recrystallization process than Ti-containing steel.

5 - Microstructural analysis (SEM/EDS, OM) supported by thermodynamic simulation indicates that Ti addition suppressed BN formation in FBT and promoted TiN/Ti(C,N), while Nb addition retained BN and is associated with the formation of Nb(C,N), predominantly at MnS/BN interfaces. These identified precipitate characteristics are consistent with and provide a microstructural basis for the higher critical strains and reduced DRX activity observed in both alloys compared to FB.

6 - OM observations and MIP analysis revealed significant refinement in FBT and FBN relative to FB. At 950 °C, FB exhibited average grain sizes of 21.9 μm (0.1 s^{-1}) and 17.7 μm (1 s^{-1}), whereas FBT and FBN were finer at 11.8/9.9 μm and 11.0/9.5 μm, respectively. At 1150 °C, FB coarsened to 33.6/31.3 μm, while FBT and FBN remained smaller at ~17–17.3/15.5–15.6 μm, nearly half the size of FB. Grain size distributions were narrower in FBT and FBN, indicating more uniform microstructures compared to the broader distribution of FB.

In summary, compared with our previous results for FB, Ti and Nb additions increased flow stresses, activation energies, and characteristic deformation parameters, while reducing DRX activity and producing finer, more homogeneous grain structures. Between the two, Ti

[DOI: 10.22068/ijmse.4448]

suppressed DRX most strongly, whereas Nb provided the greatest increase in activation energy and refinement of grain boundaries. Together, these findings demonstrate how Ti and Nb distinctly tailor the high-temperature response of boron-treated steels, establishing a direct comparison to the baseline FB alloy studied earlier.

Funding

The authors did not receive support from any organization for the submitted work.

5. References

[1] Lu, Y., "Effect of Boron on Microstructure and Mechanical Properties of Low Carbon Microalloyed Steels." McGill University, 2007, 1–15.

[2] Güler, H., Ertan, R. and Özcan, R., "Investigation of the Hot Ductility of a High-Strength Boron Steel." Mater. Sci. Eng. A, 2014, 608, 90–94.

[3] Ma, X., Miao, C., Langelier, B. and Subramanian, S., "Suppression of Strain-Induced Precipitation of NbC by Epitaxial Growth of NbC on Pre-Existing TiN in Nb–Ti Microalloyed Steel." Mater. Des., 2017, 132, 244–249.

[4] Ghosh, S., Singh, A. K., Mula, S., Chanda, P., Mahashabde, V. V. and Roy, T. K., "Mechanical Properties, Formability and Corrosion Resistance of Thermomechanically Controlled Processed Ti–Nb Stabilized IF Steel." Mater. Sci. Eng. A, 2017, 684, 22–36.

[5] Ali, M., Nyo, T., Kaijalainen, A., Javaheri, V., Tervo, H., Hannula, J., Somani, M. and Kömi, J., "Incompatible Effects of B and B+Nb Additions and Inclusions' Characteristics on the Microstructures and Mechanical Properties of Low-Carbon Steels." Mater. Sci. Eng. A, 2021, 819, 141–153.

[6] Murari, F. d., Costa, A. L. V. da, Silva, E. and Avillez, R. R., "Cold-Rolled Multiphase Boron Steels: Microstructure and Mechanical Properties." J. Mater. Res. Technol., 2015, 4, 191–196.

[7] Huang, K. and Logé, R. E., "A Review of Dynamic Recrystallization Phenomena in Metallic Materials." Mater. Des., 2016, 111, 548–574.

[8] Lin, Y. C., Chen, M. S. and Zhong, J., "Prediction of 42CrMo Steel Flow Stress at High Temperature and Strain Rate." Mech. Res. Commun., 2008, 35, 142–150.

[9] Lin, Y. C. and Chen, X. M., "A Critical Review of Experimental Results and Constitutive Descriptions for Metals and Alloys in Hot Working." Mater. Des., 2011, 32, 1733–1759.

[10] Yada, H., "Prediction of Microstructural Changes and Mechanical Properties in Hot Strip Rolling." Proc. Metall. Soc. Can. Inst. Min. Metall., 1988, 1, 105–119.

[DOI: 10.22068/ijmse.4448]

[11] Fernández, A. I., Uranga, P., López, B. and Rodriguez-Ibabe, J. M., "Dynamic Recrystallization Behavior Covering a Wide Austenite Grain Size Range in Nb and Nb–Ti Microalloyed Steels." Mater. Sci. Eng. A, 2003, 367–376.

[12] Mirghasemi, S. M., Mohammad Sharifi, E., Borhani, Gh. and Beigi, M. S., "Modelling of Hot Deformation and Dynamic Recrystallization Behavior of Boron-Bearing Low-Carbon Steel Using Hot Compression Flow Curves." Iran. J. Mater. Sci. Eng., 2024, 21, 11–29.

[13] Ronchiato, G., Castagna, M. and Colombo, R. L., "The Influence of Direct Quenching from the Forging Temperature on the Mechanical Properties of a Hardened Boron-Containing Steel." J. Heat Treat., 1985, 4.

[14] Perez, R., Garcia, A. and Juarez, J. A., "On the Structural Characteristics of Precipitates in Boron Microalloyed Steels." Scr. Metall. Mater., 1993, 28, 931–936.

[15] Juarez-Islas, J. A., Perez, R., Albarran, J. L., Flores, O. and Martinez, L., "SEM and HREM Characterization of Precipitation in a Boron Microalloyed Steel." Mater. Lett., 1994, 21, 197–202.

[16] Seto, K., Larson, D. J., Warren, P. J. and Smith, G. D. W., "Grain Boundary Segregation in Boron Added Interstitial Free Steels Studied by 3-Dimensional Atom Probe." Scr. Mater., 1999, 40, 1029–1034.

[17] Kim, S. I. and Yoo, Y. C., "Dynamic Recrystallization Behavior of AISI 304 Stainless Steel." Mater. Sci. Eng. A, 2001, 311, 108–113.

[18] Seto, K., Larson, D. J., Warren, P. J. and Smith, G. D. W., "Grain Boundary Segregation in Boron Added Interstitial Free Steels Studied by 3-Dimensional Atom Probe." Scr. Mater., 1999, 40, 1029–1034.

[19] Saha, R. and Ray, R. K., "Microstructural and Textural Changes in a Severely Cold Rolled Boron-Added Interstitial-Free Steel." Scr. Mater., 2007, 57, 841–844.

[20] Hwang, B., Suh, D. W. and Kim, S. J., "Austenitizing Temperature and Hardenability of Low-Carbon Boron Steels." Scr. Mater., 2011, 64, 1118–1120.

[21] Kim, S. I. and Lee, Y., "Influence of Cooling Rate and Boron Content on the Microstructure and Mechanical Properties of Hot-Rolled High-Strength Interstitial-Free Steels." Met. Mater. Int., 2012, 18, 735–744.

[22] Terzic, A., Calcagnotto, M., Guk, S., Schulz, T. and Kawalla, R., "Influence of Boron on Transformation Behavior during Continuous Cooling of Low-Alloyed Steels." Mater. Sci. Eng. A, 2013, 584, 32–40.

[23] Zhang, Z. G. and Xue, X. G., "Bainite Transformation of Low-Carbon and Boron-Containing Steel under Continuous Cooling." J. Iron Steel Res. Int., 2014, 21, 359–363.

[24] Li, Y. J., Ponge, D., Choi, P. and Raabe, D., "Segregation of Boron at Prior Austenite Grain Boundaries in a Quenched Martensitic Steel Studied by Atom Probe Tomography." Scr. Mater., 2015, 96, 13–16.

[25] Evans, R. W. and Scharning, P. J., "Axisymmetric Compression Test and Hot Working Properties of Alloys." Mater. Sci. Technol., 2001, 17, 995–1004.

[DOI: 10.22068/ijmse.4448]

[26] Zhao, D., "ASM Handbook: Mechanical Testing and Evaluation." ASM Int., 2000, 798–810.

[27] Shahriari, B., Vafaei, R., Sharifi, E. M. and Farmanesh, Kh., "Modeling Deformation Flow Curves and Dynamic Recrystallization of BA 160 Steel during Hot Compression." Met. Mater. Int., 2018, 24, 955–969.

[28] Humphreys, F. J. and Hatherly, M., "Recrystallization and Related Annealing Phenomena." Elsevier Science, 2004, 121–167.

[29] Christian, J. W., "The Theory of Transformations in Metals and Alloys." University of Oxford, 2002, 21–60.

[30] Rezaei, J., Parsa, M. H. and Mirzadeh, H., "Phase Transformation Kinetics of High Carbon Steel during Continuous Heating." J. Mater. Res. Technol., 2023, 27, 2524–2537.

[DOI: 10.22068/ijmse.4448]